LUND UNIVERSITY

Focused Ion Beam Preparation and Transmission Electron Microscopy of Materials for Energy Applications

Lenrick, Filip

2016

Focused Ion Beam Preparation and Transmission Electron Microscopy of Materials for Energy Applications

Filip Lenrick

Doctoral thesis

2016

LUND
UNIVERSITY

nCHREM
Centre for Analysis and Synthesis
Sweden

Akademisk avhandling som för avläggande av teknologie doktorsexamen vid tekniska fakulteten, Lunds universitet, kommer att offentligen försvaras i hörsal K:C på Kemicentrum, Naturvetarvägen 14, fredagen den 29 april 2016, kl. 13.15

Fakultetsopponent
Dr Luise Theil Kuhn, Danmarks Tekniske Universitet

Organization	Document name
LUND UNIVERSITY Centre for Analysis and Synthesis Department of Chemistry P.O. Box 124 SE-221 00 Lund, Sweden	DOCTORAL DISSERTATION Date of issue 2016-04-05
Author(s) Filip Lenrick	Sponsoring organization

Title and subtitle
Focused Ion Beam Preparation and Transmission Electron Microscopy of Materials for Energy Applications

Abstract

Throughout this thesis, samples of various materials with applications in energy converting devices have been prepared by focused ion beam machining and investigated by transmission electron microscopy. Energy converting devices can be solar cells or light emitting diodes, which turn light into electricity or vice versa. They can also be fuel cells or electrolyzer cells, which turn chemical energy into electricity or vice versa. To efficiently convert the energy, these devices require specialized materials. The results achieved by the characterization presented here include identifying twin and grain boundaries, the crystal structure and the chemical composition. The different transmission electron microscopy techniques and sample preparation methods used are explained and discussed. For example, the preparation of nanowires, which are used in solar cells and light emitting diodes, require additional steps to the standard *in-situ* lamella lift-out method. The nanowires have to be embedded in a polymer material by casting or spin coating and a frame lamella design is necessary to stabilize the thin region of interest.

Key words
Transmission electron microscopy, Focused Ion Beam, nanowires, III-V semiconductors, solid oxide fuel cells

Classification system and/or index terms (if any)

Supplementary bibliographical information	Language English
ISSN and key title	ISBN 978-91-7422-430-6
Recipient´s notes	Number of pages 230 / Price
	Security classification

Focused Ion Beam Preparation and Transmission Electron Microscopy of Materials for Energy Applications

Filip Lenrick

Doctoral thesis

2016

LUND
UNIVERSITY

nCHREM
Centre for Analysis and Synthesis
Sweden

Front cover: Top view cross-sections of radially heterostructured nanowires. Top left, top right and middle left: bright field TEM, dark field TEM and electron diffraction of InP/$Al_{0.50}In_{0.50}P$ nanowires. Middle right and bottom left: high-resolution TEM and high-angle annular dark field STEM of InP / $Al_{0.25}In_{0.75}P$ nanowires. Bottom right: conventional TEM of GaAs / $Ga_{0.55}In_{0.45}P$ nanowires.

Back cover: Side view cross-sections of $Ga_{0.81}In_{0.19}N$ nanopyramids. Top: SEM of lamella preparation by FIB. Bottom left and bottom right: high-angle annular dark field STEM and high-resolution TEM of one pyramid.

nCHREM
Centre for Analysis and Synthesis
Lund University
P.O. Box 124
SE-221 00 Lund
Sweden

ISBN 978-91-7422-430-6 (print)
ISBN 978-91-7422-435-1 (electronic)
Printed by Media-Tryck, Lund
March 2016

Abstract

Throughout this thesis, samples of various materials with applications in energy converting devices have been prepared by focused ion beam machining and investigated by transmission electron microscopy. Energy converting devices can be solar cells or light emitting diodes, which turn light into electricity or vice versa. They can also be fuel cells or electrolyzer cells, which turn chemical energy into electricity or vice versa. To efficiently convert the energy, these devices require specialized materials. The results achieved by the characterization presented here include identifying twin and grain boundaries, the crystal structure and the chemical composition. The different transmission electron microscopy techniques and sample preparation methods used are explained and discussed. For example, the preparation of nanowires, which are used in solar cells and light emitting diodes, require additional steps to the standard *in-situ* lamella lift-out method. The nanowires have to be embedded in a polymer material by casting or spin coating and a frame lamella design is necessary to stabilize the thin region of interest.

List of papers

This thesis is based on the following papers, which will be referred to in the text by Roman numerals.

I **FIB Plan and Side View Cross-Sectional TEM Sample Preparation of Nanostructures**
Filip Lenrick, Martin Ek, Daniel Jacobsson, Magnus T. Borgström, L. Reine Wallenberg
Microscsopy and Microanalysis **20** (2013) 133

II **Straight and Kinking InAs Nanowire Growth Observed *In-situ* by TEM**
Filip Lenrick, Martin Ek, Knut Deppert, Lars Samuelson, L. Reine Wallenberg
Nano Research **7** (2014) 1188

III **Phase Transformation in Radially Merged Wurtzite GaAs Nanowires**
Daniel Jacobsson, Fangfang Yang, Karla Hillerich, Filip Lenrick, Sebastian Lehmann, Dominik Kriegner, Julian Stangl, L. Reine Wallenberg, Kimberly A. Dick, Jonas Johansson
Crystal Growth & Design **15** (2015) 4795

IV **Elucidating Nucleation and Initiation of Selective Area Growth of High-Quality GaN Nanowires Serving as m-plane Substrates for Light Emitting Diodes**
Zhaoxia Bi, Martin Ek, Filip Lenrick, Rafal Ciechonski, Giuliano Vescovi, Olga Kryliouk, L. Reine Wallenberg, B. Jonas Ohlsson, Bo Monemar, Lars Samuelson
In manuscript

V **Self-Assembled InN Quantum Dots on Side Facets of GaN Nanowires**
Zhaoxia Bi, Martin Ek, Tomas Stankevic, Rainer Timm, Martin Hjort, David Lindgren, Filip Lenrick, Jonas Johansson, L. Reine Wallenberg, Anders Mikkelsen, Magnus T. Borgström, Anders Gustafsson, B. Jonas Ohlsson, Bo Monemar, Lars Samuelson
In manuscript

VI **InGaN Nano-Pyramids Grown by Selective Area Metal-Organic Vapour Phase Epitaxy**
Zhaoxia Bi, David Lindgren, Filip Lenrick, Anders Gustafsson, L. Reine Wallenberg, Bo Monemar, Lars Samuelson
In manuscript

VII **Electron Microscopy Study of Single Crystal $BaZr_{0.9}Y_{0.1}O_{3-x}$ Films Prepared by Chemical Solution Deposition**
Filip Lenrick, David Griesche, Jae-Wuk Kim, Theodor Schneller, L. Reine Wallenberg
ECS Transactions **45** (2012) 121

VIII **$LaCoO_3$: Promising Cathode Material for Protonic Ceramic Fuel Cells Based on a $BaCe_{0.2}Zr_{0.7}Y_{0.1}O_{3-\delta}$ Electrolyte**
Sandrine Ricote, Nikolaos Bonanos, Filip Lenrick, L. Reine Wallenberg
Journal of Power Sources **218** (2012) 313

IX **Synthesis by Spark Plasma Sintering of a Novel Protonic/Electronic Conductor Composite: $BaCe_{0.2}Zr_{0.7}Y_{0.1}O_{3-\delta}$ / $Sr_{0.95}Ti_{0.9}Nb_{0.1}O_{3-\delta}$ (BCZY27 / STN95)**
Jason S. Fish, Sandrine Ricote, Filip Lenrick, L. Reine Wallenberg, Tim C. Holgate, Ryan O'Hayre, Nikolaos Bonanos
Journal of Materials Science **48** (2013) 6177

X **Chemical Solution Deposition of Thin Films for Protonic Ceramic Fuel Cells**
Per Martin Rørvik, Camilla Haavik, David Griesche, Theodor Schneller, Filip Lenrick, L. Reine Wallenberg
Solid State Ionics **262** (2014) 852

My contributions

I I proposed and performed the novel sample preparation methods on the provided samples. I acquired the SEM, STEM, HRTEM, DFTEM images, XEDS measurements, and performed the image and XEDS analysis. I was the main author of the paper.

II I built the cells used for the *in-situ* nanowire growth experiments. There was equal contribution from myself and M. Ek with regard to designing the cell, carrying out the experiments, acquiring the SEM, STEM, HRTEM images, XEDS measurements, and analyzing the data. I was the main author of the paper.

III I performed the FIB sample preparation, acquired the TEM, STEM, DFTEM and HRTEM images, SAED patterns, and analyzed the data.

IV I performed the FIB sample preparation, acquired the TEM images of the FIB lamellae, and analyzed the data.

V I performed the FIB sample preparation, acquired the TEM images of the FIB lamellae, and analyzed the data. I built plausible InN–GaN interface models.

VI I performed the FIB sample preparation, acquired the TEM images, SAED patterns, and analyzed the data.

VII I performed the FIB sample preparation, acquired the SEM, HRTEM and STEM images, and analyzed the data. I acquired EFTEM images and analyzed the EFTEM data together with C. J. D. Hetherington. I was the main author of the paper.

VIII I performed the FIB sample preparation. I acquired the TEM, STEM images, XEDS measurements, and analyzed the data.

IX I performed the FIB sample preparation, acquired the HRTEM, STEM images, SAED patterns, XEDS measurements, and analyzed the data.

X I performed the FIB sample preparation, acquired the TEM, HRTEM, STEM images, and analyzed the data.

Papers not included in the thesis:
I contributed to the following papers which are beyond the scope of this thesis.

xi **High-Frequency Performance of Self-Aligned Gate-Last Surface Channel MOSFET**
Mikael Egard, Lars Ohlsson, Mats Ärlelid, Karl-Magnus Persson, B. Mattias Borg, Filip Lenrick, Reine Wallenberg, Erik Lind, Lars-Erik Wernersson
Electron Device Letters, IEEE **33** (2012) 369

xii **Performance of ZrO 2-Supported Nb-and W-oxide in the Gas-Phase Dehydration of Glycerol to Acrolein**
Mariano Massa, Arne Andersson, Elisabetta Finocchio, Guido Busca, Filip Lenrick, L. Reine Wallenberg
Journal of Catalysis **297** (2013) 93

xiii **Characterization of White Layer Generated when Turning Aged Inconel 718**
Volodymyr Bushlya, J.M. Zhou, Filip Lenrick, Pajazit Avdovic, Jan-Eric Ståhl
Procedia Engineering **19** (2011) 60

xiv **Growth Parameter Design for Homogeneous Materials Composition in Ternary $Ga_xIn_{1-x}P$ Nanowires**
Alexander Berg, Filip Lenrick, Neimantas Vainorius, Jason P. Beech, L. Reine Wallenberg, Magnus T. Borgström
Nanotechnology **26** (2015) 435601

xv **Direct Growth of GaN Nanowires on Silicon (111) by Metalorganic Vapour Phase Epitaxy**
Rafal R. Ciechonski, Filip Lenrick, Bo Monemar, Reine Wallenberg, B. Jonas Ohlsson, Lars Samuelson
Extended abstract: European Workshop on Metalorganic Vapour Phase Epitaxy (2015)

Abbreviations

ADF	annular dark field
BF	bright field
BFTEM	bright field transmission electron microscopy
CSD	chemical solution deposition
DFTEM	dark field transmission electron microscopy
DP	diffraction pattern
eV	electronvolt
FIB	focused ion beam
GPA	geometric phase analysis
HAADF	high-angle annular dark field
HRTEM	high-resolution transmission electron microscopy
LT	lateral twin
IGT	intergrowth twin
INLO	*in-situ* lamella lift-out
IT	inclined twin
LAADF	low-angle annular dark field
LED	light emitting diode
MOVPE	metalorganic vapor phase epitaxy
OL	objective lens
PT	perpendicular twin
PC-SOEC	proton-conducting solid oxide electrolyzer cell
PC-SOFC	proton-conducting solid oxide fuel cell
pCTF	phase contrast transfer function
ROI	region of interest
SA	selected area
SAED	selected area electron diffraction
SPS	spark plasma sintering
SEM	scanning electron microscopy
STEM	scanning transmission electron microscopy
TEM	transmission electron microscopy
TPB	triple phase boundary
TS	thick section
VLS	vapor–liquid–solid
XEDS	X-ray energy dispersive spectroscopy, or spectrum

Symbols

A_{OL}	objective lens aperture
A_{SA}	selected area aperture
$\arg(\psi)$	argument of ψ
$\mathcal{C}$	image contrast function
$\mathrm{C_S}$	spherical aberration constant
χ	total phase error
χ_{CS}	phase error due to spherical aberration
χ_{df}	phase error due to defocus
d	interplanar distance
e^-	electron
$\mathcal{F}$	Fourier transform
$\mathcal{F}^{-1}$	inverse Fourier transform
g	diffraction spot
h	Planck's constant
III–V	semiconductor of elements from groups 13 and 15 (IUPAC)
ν	the frequency of a photon
P_g	geometric phase
ψ	electron wavefunction
Ψ_{bfp}	electron wavefunction in the back focal plane of the OL
ψ_i	electron wavefunction in the image plane of the OL
ψ_{ill}	electron wavefunction before the object plane of the OL
ψ_o	electron wavefunction in the object plane of the OL
$\square$	vacancy on an oxygen site
V_t	projected potential
(ad)	state of matter: adsorbed
(g)	state of matter: gas
(h, k)	coordinates in reciprocal space
(l)	state of matter: liquid
(s)	state of matter: solid
(x, y)	coordinates in real space
$\lvert\psi\rvert$	absolute value (or modulus) of ψ
2H	wurtzite crystal structure
3C	zinc blende (sphalerite) crystal structure
4H	carborundum polytype (III)

Contents

1 Introduction

> *We've got to find a way to make this, fit into the hole for this ...using nothing but that.*
>
> — NASA technician [1]

In these studies, electron microscopy was used to characterize various materials with applications in energy conversion. Especially transmission electron microscopy (TEM) of specimens prepared by focused ion beam (FIB) machining was used. The transmission electron microscope is powerful enough to both resolve and identify individual atoms [2, 3] while at the same time being versatile enough for general characterization [4, 5]. The major downside is the strict requirement on the specimens, which must be electron transparent. This is where the FIB process becomes useful with its ability to prepare thin specimens from almost any material and sample.

This chapter will give a brief introduction to two applications of the studied materials: conversion between light energy and electrical energy, exemplified by solar cells and light-emitting diodes (LEDs), and conversion between chemical energy and electrical energy, exemplified by fuel cells and electrolyzer cells. More thorough introductory texts can be found in the textbooks by Sze [6] and by Larminie and Dicks [7] on photonic and electrochemical devices, respectively.

Photonic devices

As a point of reference, the electromagnetic radiation released by the sun carries most of the energy in the band from infrared to ultraviolet. This corresponds to wavelengths from about 3000 nm to about 200 nm, or photon energies from about 0.4 eV to about 6 eV.

The two photonic phenomena that are relevant here are absorption and spontaneous emission in semiconductors. Absorption takes place when the solid is illuminated and electron–hole pairs are created, as illustrated in Figure 1.1a. If the photon energy is equal to, or larger than, the bandgap energy the

absorption occurs by an *intrinsic transition*. If the bandgap energy is too high for the photon, it can only be absorbed by an *extrinsic transition* when there are available energy levels in the, usually forbidden, bandgap. These extra levels are often caused by chemical impurities or crystal defects. The extrinsic transitions can lead to reduced device efficiency when unwanted, but can also be utilized for their special properties. Spontaneous emission is the reverse process of absorption in that the merger of a conduction band electron and a valence band hole give rise to the emission of a photon with an energy equal to the bandgap, see Figure 1.1b.

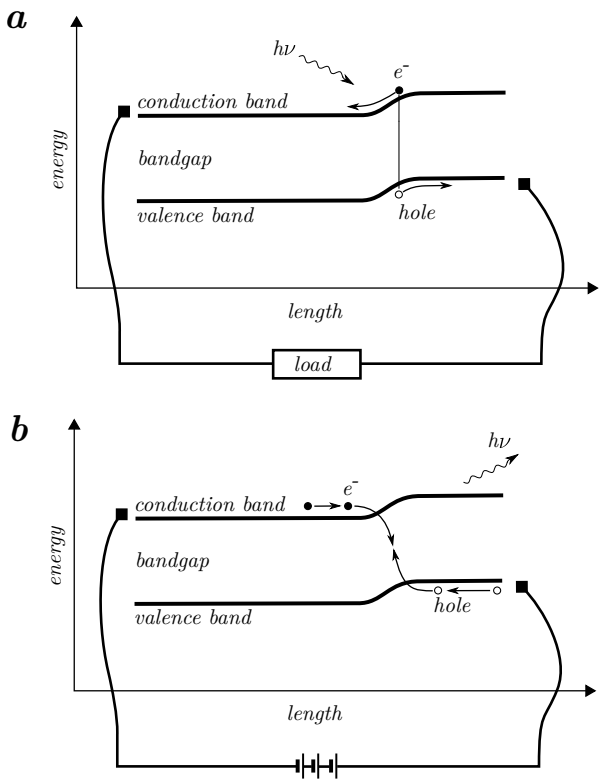

Figure 1.1: Energy band diagram for a solar cell (a) and a light emitting diode (b) at the p-n junction. (a) A photon with energy $h\nu$, corresponding to the bandgap energy, is absorbed and excites an electron to the conduction band leaving a hole in the valence band. The band structure of the p-n junction helps separate the charges. (b) An external source of power pulls electrons out from the p-side, leaving holes behind, and injects electrons into the n-side. The electrons and holes recombine at the p-n junction where a photon, with energy ($h\nu$) equal to the bandgap energy, is released through spontaneous emission.

Different semiconductors can have different bandgap energies and types of bandgap. For instance, GaAs-based LEDs emit infrared light (about 900 nm) since the bandgap is 1.4 eV, while certain SiC-based LEDs emit blue light (about 400 nm) since the bandgap is 3.1 eV. However, the *indirect bandgap* in SiC gives rise to a low brightness, making SiC-based LEDs hard to commercialize. For commercial blue-light LEDs, GaN seems to hold most promise with its *direct bandgap* of 3.4 eV. By tuning the stoichiometry of the binary, ternary and quaternary compounds in the (Al, Ga, In)N system [IV-VI], efficient LEDs emitting light with any wavelength from 200 nm to 600 nm could potentially be manufactured. One major hurdle, however, is the lack of lattice-matched substrates. Strain-relieving defects are normally spawned at the interface between two materials with different lattice parameters, leading to extrinsic transitions and a low device efficiency.

One route around the problem of lattice-matching is to use the nanowire technology. Many troublesome interfaces can be made completely free from defects in thin nanowires since the interface area is small with no surrounding bulk. Nanowire engineers can also use masks and special morphologies to keep defects from entering the active volume [8, 9, IV].

The solar cell is in many ways similar to the LED, but instead of converting electrical energy into light, it turns light energy into electricity. It does so by separating electrons and holes over a p-n junction (the interface between semiconductors with positively charged carriers and negatively charged carriers) when photons are absorbed. A solar cell would ideally convert all the photon energy to electricity, but only a single bandgap energy is ideally matched to each wavelength. Photons with energies lower than the bandgap do not contribute to cell output while all energy higher than the bandgap is wasted as heat. One solution to this problem is the tandem solar cell geometry where different materials are combined to provide many distinct bandgap energies. The binary, ternary and quaternary compounds in the (Al, Ga, In)(P, As, Sb) system [I-III] are ideal for tandem solar cells as these semiconductors provide bandgaps from about 0.2 eV (6000 nm) to 2.5 eV (500 nm) and have similar lattice parameters. One problem, however, is that these materials are expensive and large quantities of material are needed in the production of thin film solar panels. This problem can be overcome by the nanowire technology where less material is needed. Other benefits are that expensive lattice-matched substrates can be replaced by cheaper ones and that the morphology and geometry can be fine-tuned to increase the efficiency [10, 11].

Electrochemical devices

Electrochemical cells convert energy stored in chemical form to electricity, or vice versa, through chemical redox reactions. The redox reaction that is relevant here is the one involving hydrogen, oxygen and water:

$$2H_2 + O_2 \rightleftharpoons 2H_2O \tag{1.1}$$

For proton-conducting solid oxide fuel cells (PC-SOFCs) [VII, VIII, X] and proton-conducting solid oxide electrolyzer cells (PC-SOECs), the reaction is better described in half cell form:

$$\text{Hydrogen electrode}: \quad 2H_2 \rightleftharpoons 4H^+ + 4e^- \tag{1.2}$$

$$\text{Air electrode}: \quad O_2 + 4H^+ + 4e^- \rightleftharpoons 2H_2O \tag{1.3}$$

For fuel cells, it is the overall oxidation (right arrow in reaction 1.1) that drives the energy conversion. The device works by forcing the electrons and protons formed at the hydrogen electrode (reaction 1.2) to take different routes to the air electrode. The electrons move in an external circuit, where the electrical energy can be put to use, while the protons go through the electrolyte, as shown in Figure 1.2a. In the electrolyzer mode, the reduction reaction (left arrow in reaction 1.1) is driven by an external power source, schematically drawn in Figure 1.2b.

The proton conducting materials used in these devices are often perovskites with the chemical formula ABO_3 where A is commonly Ba or Sr, and B is usually Zr or Ce, in addition to some trivalent dopant such as Y, Gd, Nd, or La. $BaCeO_3$-based materials have the highest conductivity among these proton conductors, but due to poor chemical stability (it decomposes into $BaCO_3$ and CeO_2 in the presence of CO_2), it is not suitable for practical use [12–14]. Many materials based on Y-doped $BaZrO_3$ exhibit satisfactory proton conductivity in addition to being mechanically and chemically stable under operational conditions (i.e. at high temperatures and in the presence of CO, CO_2, H_2O and H_2S) [15, 16].

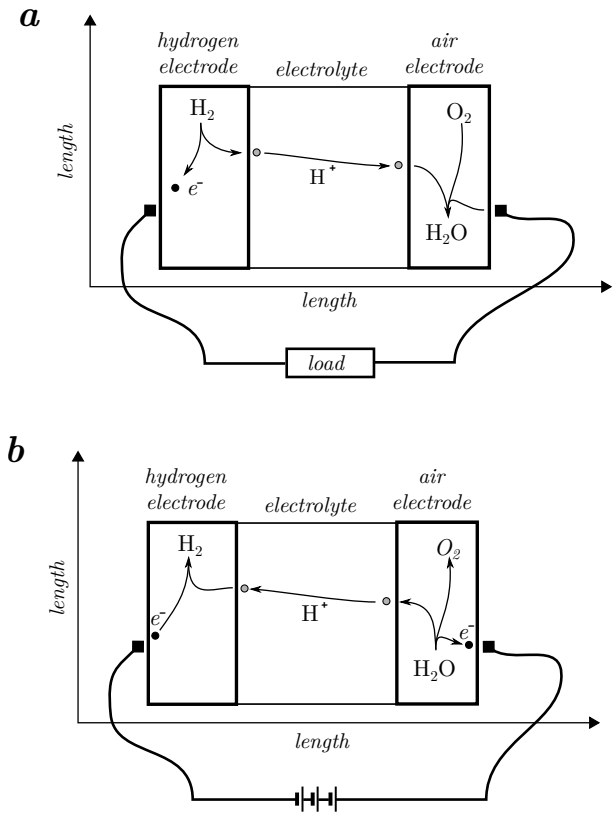

Figure 1.2: Element flow and charge flow for a proton-conducting fuel cell (a) and proton-conducting electrolyzer cell (b). (a) Hydrogen is split into protons and electrons in the hydrogen electrode. Both electrons and protons are pulled towards the air electrode as a result of the overall oxidation reaction. Electrons are forced to go via an external circuit, where they perform electrical work, and protons are forced to go through the electrolyte. In the air electrode, protons, electrons, and oxygen react to form water. (b) An external source of power drives the reduction reaction. Water is split into oxygen, protons and electrons in the air electrode. The protons go through the electrolyte to the hydrogen electrode, where they combine with electrons from the external circuit to form hydrogen.

The proton conduction mechanism is here explained using Y-doped $BaZrO_3$, as illustrated in Figure 1.3. An oxygen vacancy is formed in the solid after two tetravalent Zr ions have been substituted by two trivalent Y ions:

$$2Zr^{4+}\ (s) + O^{2-}\ (s) \leftrightarrow 2Y^{3+}\ (s) + \square \tag{1.4}$$

Where $\square$ stands for the vacancy on an oxygen site. In a wet atmosphere, a water molecule settles on the oxygen vacancy and forms two hydroxide ions, each with a loosely bound hydrogen ion (proton):

$$H_2O\ (g) + \square + O^{2-}\ (s) \leftrightarrow 2OH^{-}(s) \tag{1.5}$$

The protons can then move along the lattice by *hopping* from oxygen site to oxygen site, thus breaking and re-forming bonds sequentially.[17–19]

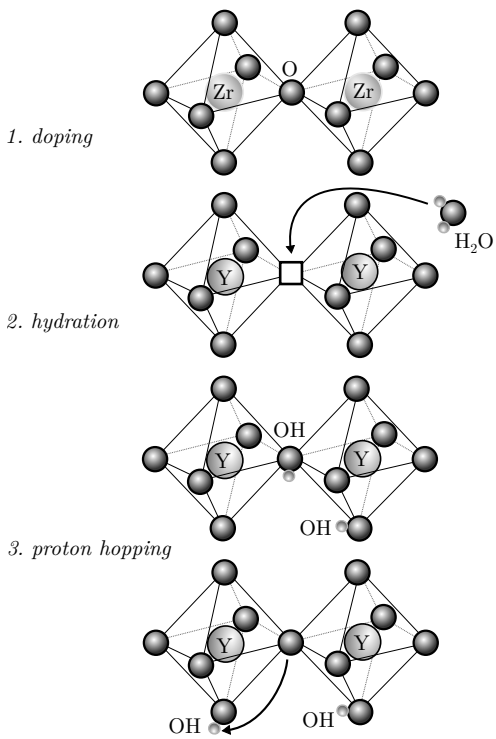

Figure 1.3: Proton conductivity in Y-doped $BaZrO_3$. Oxygen vacancies are formed to keep the material charge neutral when doped. Water molecules are incorporated and form hydroxide ions. The hydrogen ions (protons) are free to move (*hop*) from oxygen site to oxygen site.

Another device that should be mentioned is the hydrogen separation membrane, which extracts hydrogen from gas mixtures [IX]. On such membranes, H_2 is oxidized to protons and electrons which dissolve into the material. When reduced on the opposite side of the membrane, H_2 is separated from other gas species. The partial pressure gradient of hydrogen is used as the driving force. These devices are often made of composites where the conduction of protons and electrons are in two different phases.[20–22]

2 Crystal Structures and Synthesis

> *Fourier analysis is central in solving many scientific and engineering problems.*
>
> — Bill Hammack [23]

This chapter discusses crystal structures and synthesis methods. The semiconductor materials, synthesized here using *metal-organic vapor phase epitaxy*, mainly belong to the wurtzite and zinc blende (or sphalerite) structure family, while the solid oxide material, synthesized here by *chemical solution deposition* and *spark plasma sintering*, mainly belong to the perovskite family.

Crystal Structures

The general formula for wurtzite and zinc blende is AB, where one atom type forms close-packed layers, as in Figure 2.1, and the other atom occupies half of the tetrahedral interstitial sites. Either atom A or B can be viewed as the element forming the layers. The difference between wurtzite and zinc blende is the stacking sequence. A layer can be in one of three positions (labeled a, b and c) with respect to a neighboring layer (the stacking sequence affects both the electronic structure and bandgap [24,25]). In wurtzite, two types of layers repeat as $...ababab...$, while in zinc blende the sequence is $...abcabc...$ with three repeating layers. Many other sequences occur, such as $...abcbabcba...$ which is called *4H* (Ramsdell notation) since it is a stacking of four layers and the resultant structure has a hexagonal symmetry. In the same notation, wurtzite translates to *2H* and zinc blende to *3C*, where *C* stands for cubic.[26] Note, however, that the layers are actually bilayers consisting of two types of atoms. Using GaAs as an example material, and writing the As layer positions as superscript on the Ga layer positions, *2H* becomes $...a^b\ b^a\ a^b\ b^a...$ and *3C* becomes $...a^b\ b^c\ c^a\ a^b\ b^c\ c^a....$ Every Ga layer has a neighboring As layer with an identical position.

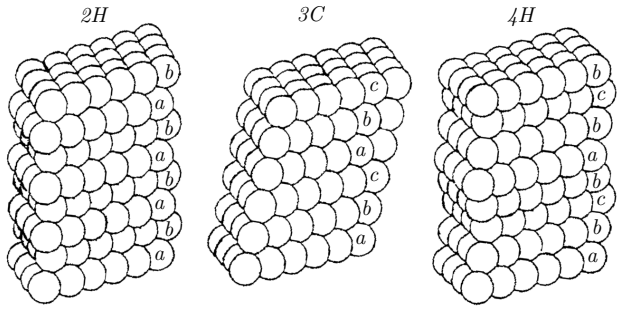

Figure 2.1: Three stacking sequences of close-packed layers and their Ramsdell notation. Figure adapted from [26].

The general formula for *perovskite* is ABO_3 where oxygen ions form a cubic network of corner-sharing octahedra with B ions in the octahedra and A ions in the cubeoctahedral sites, drawn in Figure 2.2a. The cubic symmetry is often reduced, however, giving larger tetragonal or orthorombic unit cells. This reduction of symmetry is related to the size of the cations where certain ions, or combinations of ions, cause the octahedra to tilt as shown in Figure 2.2b-c.[26]

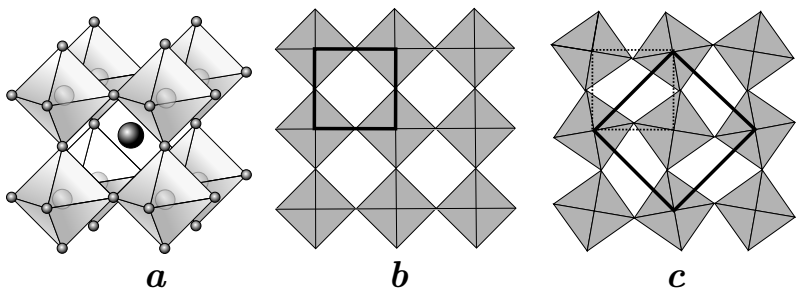

Figure 2.2: (a) Coordination polyhedra model of perovskite (ABO_3). The large dark sphere is A, the small spheres are O and the spheres inside the octrahedra are B. (b) Side view projection of the network of corner-sharing octahedra in the cubic structure. (c) The network of corner-sharing octahedra in a tetragonal structure where the octahedra are tilted. The unit cells are outlined by solid lines.

Since the TEM images are recorded as plane projection of the samples, projection models in combination with 3D models are helpful for understanding the crystal structure. Such illustrations for perovskite, *2H*, *3C*, and *4H* are shown in Figure 2.3.

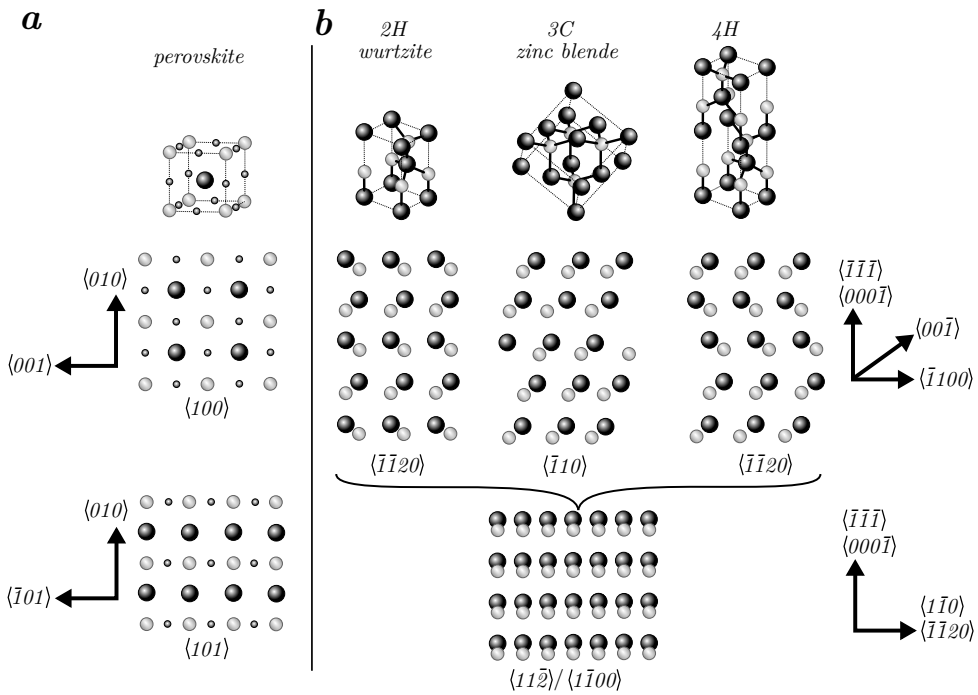

Figure 2.3: Unit cells and projection models of the perovskite structure and three important binary semiconductor structures. (a) The cubic perovskite unit cell and projections in $\langle 100 \rangle$ and $\langle 101 \rangle$. (b) The unit cells for *2H* (wurtzite), *3C* (zinc blende) and *4H*. The $\langle \bar{1}10 \rangle$ / $\langle \bar{1}\bar{1}20 \rangle$ projections are often used in TEM to identify the structure, the presence of stacking faults and twins, while in the $\langle 11\bar{2} \rangle$ / $\langle 1\bar{1}00 \rangle$ projections these features cannot be observed. Note that the (111)/(0001) and $(\bar{1}\bar{1}\bar{1})/(000\bar{1})$ surfaces are polar and terminated by a single atom type.

Synthesis

In *metal-organic vapor phase epitaxy* (MOVPE) [27, 28] precursor gases, typically metal-organic or hydride compounds in H_2, are brought to a heated substrate where they crack and form organic and semiconductor species. As an example, the overall chemical reaction of GaAs is:

$$Ga(CH_3)_3\,(g)\ +\ AsH_3\,(g) \rightarrow 3CH_4\,(g)\ +\ GaAs\,(s) \tag{2.1}$$

The organics follow the carrier gas out of the chamber while the semiconductor species combine into a solid material. One way to synthesize nanowires is to cover the substrate with a mask layer, typically Si_3N_4 or SiO_2, on which the nanowires grow through small openings. Such nanowires are shown in Figure 2.4b. Another way is to suppress normal film epitaxy by keeping the conditions in the chamber below certain thresholds, (e.g. below a system dependent temperature). Nanowires can grow under such inhibited conditions with the aid of seed particles, usually Au, in a catalyzed process known as vapor–liquid–solid (VLS). A nanowire grown by VLS is shown in Figure 2.4a. The seed particle size and location determine the diameter and position of the nanowire. Different precursors give rise to different materials and it is possible to form heterostructures by switching gases mid-synthesis. The addition of new material can be limited to obtain growth under the seed particle, forming *axial heterostructures*, or growth as a film around the entire nanowire, forming *radial heterostructures*.

In *chemical solution deposition* (CSD) [29,30] a solution of precursor compounds are added to a substrate. Different ways of adding the solution give rise to different film morphologies, such as dense films, porous films or in the form of nanoparticles, as shown in Figure 2.5. The highest temperature used in CSD is usually between 500°C and 1000°C which is lower than more conventional (sintering) methods where temperatures often exceed 1000°C. The low sintering temperature used in CSD reduces the risk of interdiffusion between different materials and therefore increases the number of compatible materials in a device. The process can be summed up in four steps: 1) Precursors, typically metal-organic compounds, are mixed in stoichiometric ratio in a solvent. 2) Coating of a substrate, either by i) spin coating using a spinner, ii) spray coating using a misted solution, iii) dip coating in a solution bath, or iv) infiltration in a porous structure. 3) Exposure of the wet film to multiple steps of thermal processing, usually on a hot plate and in an oven. The aim is to evaporate solvents, remove organic species and crystallize the material. 4) Iteration of the coating and thermal processing in order to achieve the desired film morphology and thickness.

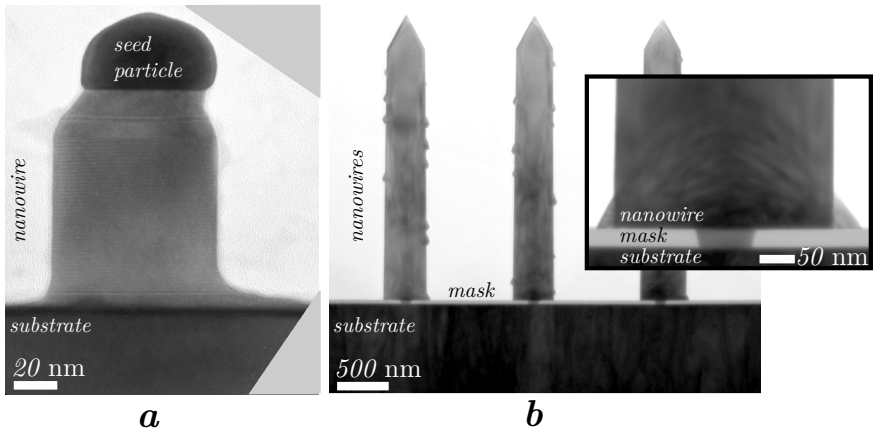

Figure 2.4: Nanowires grown by metal-organic vapor phase epitaxy. (a) GaAs nanowire grown by Au seeded vapor–liquid–solid on a GaAs substrate [III]. Specimen prepared by focused ion beam and imaged by transmission electron microscopy. (b) GaN nanowires (with InN dots on the facets) grown through small openings in a Si_3N_4 mask on a GaN substrate [V]. Inset is a higher magnification image of the interface region. Specimen prepared by focused ion beam and imaged by transmission electron microscopy.

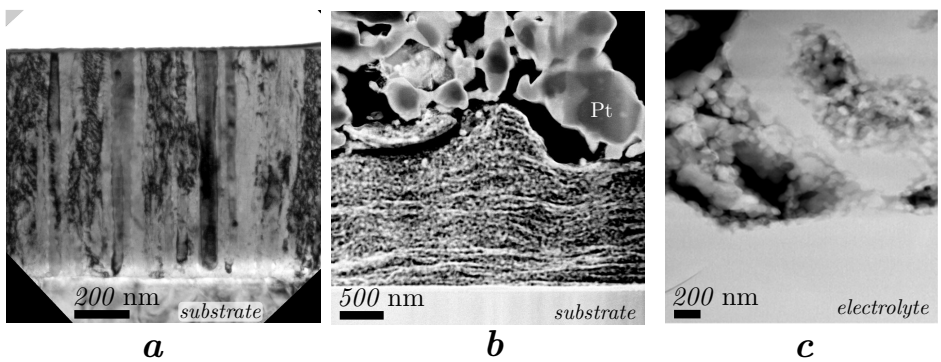

Figure 2.5: Three morphologies synthesized by chemical solution deposition. (a) Dense $BaZr_{0.9}Y_{0.1}O_3$ with columnar grains [X]. The proton-trapping grain boundaries were eliminated from through-plane direction with these *bamboo*-structured electrolytes [31]. Synthesized by spin coating on a NiO substrate, specimen prepared by focused ion beam and imaged by transmission electron microscopy. (b) Porous $La_{0.6}Sr_{0.4}Fe_{0.8}Co_{0.2}O_3$ with porous Pt. Synthesized by spray coating on a Gd-doped CeO_2 substrate, specimen prepared by focused ion beam and imaged by scanning transmission electron microscopy. (c) Nanosized $LaCoO_3$ particles in a porous structure of $BaCe_{0.2}Zr_{0.7}Y_{0.1}O_3$, on a dense $BaCe_{0.2}Zr_{0.7}Y_{0.1}O_3$ electrolyte [VIII]. Synthesized by infiltration, specimen prepared by focused ion beam and imaged by scanning transmission electron microscopy.

Spark plasma sintering (SPS) [32,33] is not a synthesis method, but rather a sintering technique, since it requires a powder of the material or materials. The powder can be synthesized by, for example, a solid-state reaction of precursor oxides and carbonates. The sintering process can be broken up into several steps: 1) The powder is arranged as a pellet in a die (typically made of graphite), and placed in vacuum or an inert atmosphere. 2) The die is then put under uniaxial pressure. 3) A direct current is applied through the die in a number of pulses. The role of the current is twofold as it provides both a thermal effect (Joule heating) and an increased mass transport. The mass transport effect is attributed to i) an *electron wind* modifying the diffusion flux, ii) an increase of point defects, or iii) a lowering of the activation energy for defect mobility. Whether a plasma is formed between the powder particles is controversial. Compared to more conventional methods, there are some advantages of using SPS for obtaining dense material (such as shown in Figure 2.6). For example, SPS offers high heating rates (up to 1000°C/min), a lower sintering temperature (by several hundreds of degrees) and shorter holding times (as short as a few minutes in total). Very fine powders can be sintered with little grain growth due to limited Oswald ripening. Even though a uniaxial pressure is applied, a pseudo-isostatic pressure can be achieved in SPS when the sample is embedded in conducting and pressure-transmitting die material.

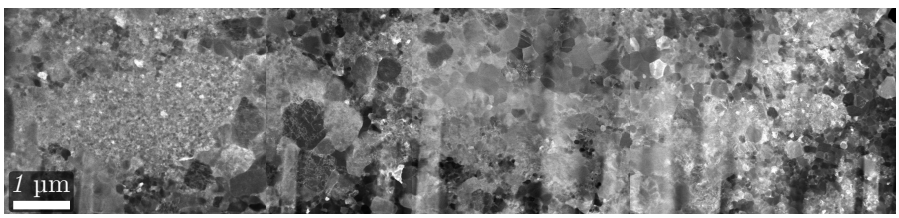

Figure 2.6: A dense composite membrane, for hydrogen separation application, sintered by spark plasma sintering (SPS) [IX]. The two phases were $BaCe_{0.2}Zr_{0.7}Y_{0.1}O_3$ and $Sr_{0.95}Ti_{0.9}$-$Nb_{0.1}O_3$, synthesized by a solid-state reaction from oxide and carbonates precursors. The specimen was prepared by focused ion beam and imaged by scanning transmission electron microscopy.

3 Transmission Electron Microscopy

Doesn't this look a bit like the patterns on a cow?

— Alan Turing [34]

The aim of this chapter is to provide an overview of the transmission electron microscope and image formation. Extensive introductions to the subject can be found in the textbooks by Fultz and Howe [35] and Williams and Carter [4]. Since a JEOL 3000F was the transmission electron microscope used for these studies, the text will primarily be relevant for that instrument, or similar ones.

The transmission electron microscope has two basic modes. In conventional transmission electron microscopy (TEM) the beam is broad and stationary, while in scanning transmission electron microscopy (STEM) the beam is focused and scanned in a raster pattern. In TEM, the image is recorded in parallel on a 2D detector, and in STEM the image is recorded by serial acquisition.

Hardware

The transmission electron microscope can be thought to have three units: the illumination system, the image formation system and the projection system. In the *illumination system*, electrons are extracted from a heated Schottky emitter and adjusted to illuminate the sample either with a close to parallel beam of electrons (in TEM mode) or a convergent spot-beam (in STEM mode). A high brightness and a low energy spread are attributes of a good electron gun. However, technical issues such as stability over time and vacuum dependence are also considered. A medium acceleration voltage transmission electron microscope typically uses 300 kV to accelerate the electrons, which gives them a wavelength of about 1.97 pm. The *image formation system* plays a dominant role in the theory of high-resolution TEM imaging. The objective lens (OL) is used to form both images and diffraction patterns (or optical

Fourier transforms). The selected area (SA) aperture is used to select the region of interest of the sample and the objective lens aperture is used to select the region of interest in the diffraction pattern. The sample holder has the ability to move and tilt the sample which is useful for aligning a crystal zone axis with the electron beam. In STEM mode the *image formation system* and the *projection system* are combined. Lenses are used to set the camera length (the magnification of the diffraction pattern in the detection plane), and hence the range of scattering angles detected. In TEM mode, the *projection system* magnifies and projects the image or diffraction pattern onto a phosphorescent plate, for quick viewing, or a camera sensor for image acquisition. The size, density and total number of the sensor pixels influence the acquisition time, field of view and image resolution.

TEM imaging and diffraction

Information about the sample is interpreted from contrast, i.e., the relative differences in intensity between two adjacent regions of an image or diffraction pattern. The mechanism for contrast formation and its interpretation are the subject of the next part of this chapter.

SAED, BFTEM, DFTEM and HRTEM

If we assume that a parallel beam of coherent electrons is used in TEM mode we can build a *simplistic* model of diffraction and image formation. In the electron wavefunction notation, $\psi_z(x, y)$, z denotes a plane perpendicular to the optical axis and (x, y) are real space coordinates. Every defined point has an amplitude, $|\psi|$, and a relative phase shift, $\arg(\psi)$, also known as the phase.

$$\psi = |\psi| \, e^{-i \arg(\psi)} \tag{3.1}$$

A graphical representation of the model is presented in Figure 3.1 and more information about the model can be found in [36]. It is important to note that the image intensity – or contrast, $\mathcal{C}$ – is not directly proportional to the phase, $\arg(\psi)$, but to the amplitude squared, $\mathcal{C} \propto |\psi|^2$. Phase changes are caused by all samples while a change in amplitude is mainly the result of heavy atoms or thick samples. Heavy (positively charged) atom-nuclei have a strong pull and can sling (negatively charged) electrons far off axis. The thicker the sample, the more opportunities there are for this to happen. This results in a *mass/thickness contrast*, which is one contribution to the contrast seen in bright field (BF)TEM images. The other contribution to contrast is *diffraction contrast* which is due to shifts in phase, and the following text

will assume that phase change is the sole effect on the electrons during beam-sample interaction.

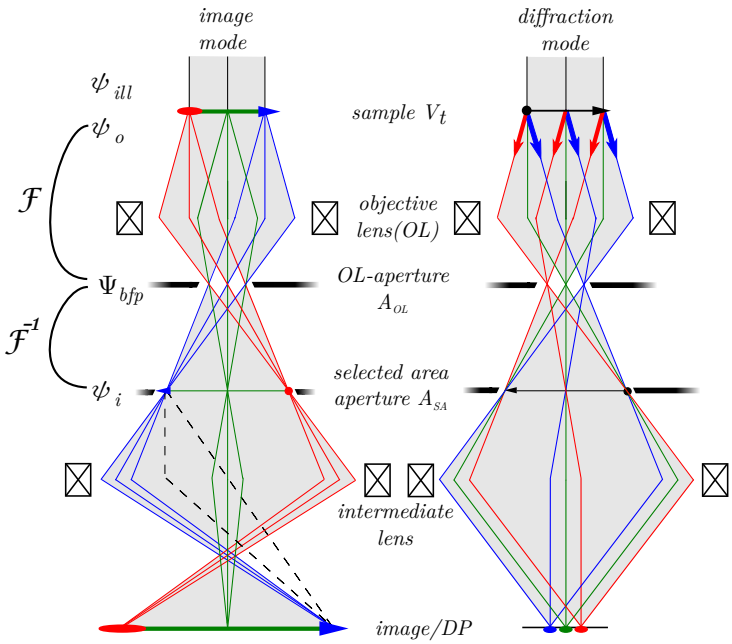

Figure 3.1: Electron wavefunction notation and ray diagrams for the *image formation system* in both image mode and diffraction mode. The intermediate lens changes the focal length in order to place either the image plane of the objective lens (ψ_i) or back focal plane (Ψ_{bfp}) in the object plane of the projector lens, which is at the bottom of the illustration. The illumination is parallel and coherent ($\psi_{ill} = 1$) and the phase in the exit wavefunction (ψ_o) depends on the projected sample potential (V_t). The color coding in image mode (left) refers to the position on the specimen, while the color coding in diffraction mode (right) refers to the diffraction angle.

Changes in phase rely on different optical pathways for the beam-electrons going through atoms and the beam-electrons going in-between atoms. This phase change depends linearly on the projected potential of the sample, V_t, according to the *weak phase object approximation*. The beam that has just passed through the sample, known as the exit wavefunction ψ_o, will thus carry information about V_t (including atom positions) in its phase since $\arg(\psi_o) \propto V_t$. Simplified to:

$$\psi_o = e^{-i\,V_t} \tag{3.2}$$

It is now the task of the lower part of the microscope to make the information in $\arg(\psi_o)$ detectable. Four common ways of doing this include selected area electron diffraction (SAED), bright field-, dark field-, and high-resolution transmission electron microscopy (BFTEM, DFTEM and HRTEM). For each of these techniques, interpretation is made by linking the image contrast, $\mathcal{C}$, to the sample, V_t, via the exit wavefunction, ψ_o.

The sample sits in the object plane of the objective lens (OL). A Fourier transform of the object plane is formed in the back focal plane, $\mathcal{F}(\psi_o) = \Psi_{bfp}$, while an image of the object plane is formed in the image plane, which can be seen as an inverse Fourier transform of the back focal plane, $\mathcal{F}^{-1}(\Psi_{bfp}) = \psi_i$.

In SAED [III, IX], the selected area aperture, A_{SA}, is inserted in a conjugate image plane to isolate the area of interest of the sample. It is only this isolated area that contributes to the Fourier transform projected onto the camera. Information about the sample will thus be visible in reciprocal form as a diffraction pattern. In our model the selection is made directly in the object plane:

$$\mathcal{F}(\ A_{\mathrm{SA}}\ \psi_o(x,y)\ ) = \Psi_{bfp}(h,k) \tag{3.3}$$

$$A_{\mathrm{SA}}(x,y) = \begin{cases} 1 & \textit{if } (x,y) \textit{ are inside the aperture} \\ 0 & \textit{if } (x,y) \textit{ are outside the aperture} \end{cases} \tag{3.4}$$

Here, (h,k) are coordinates in reciprocal space. If, instead of the back focal plane, the image plane is projected onto the camera sensor, no contrast appears as $|\psi_i| = |\psi_o| = 1$. Contrast can be achieved by introducing an objective lens aperture, A_{OL}, in the back focal plane:

$$\mathcal{F}^{-1}(A_{\mathrm{OL}}\ \Psi_{bfp}(h,k)) = \psi_i(x,y) \tag{3.5}$$

$$A_{\mathrm{OL}}(h,k) = \begin{cases} 1 & \textit{if } (h,k) \textit{ are inside the aperture} \\ 0 & \textit{if } (h,k) \textit{ are outside the aperture} \end{cases} \tag{3.6}$$

In BFTEM [I-VII, IX-X], only electrons from the centermost region of the back focal plane are allowed to pass, and the electrons in the outer region are excluded from the image. Areas of the sample that diffract strongly are darker in the image, which is the mechanism for diffraction contrast. In DFTEM [I,

III], electrons from a different region, or scattering angle, in the back focal plane is allowed to pass and the sample areas that scatter in the selected angle are bright in the image. MatLab simulations of ψ, as defined here, are shown in Figure 3.2. The simulations are in one dimension and should be interpreted as phase or amplitude on the y-axis for a line across the wavefunction surface on the x-axis.

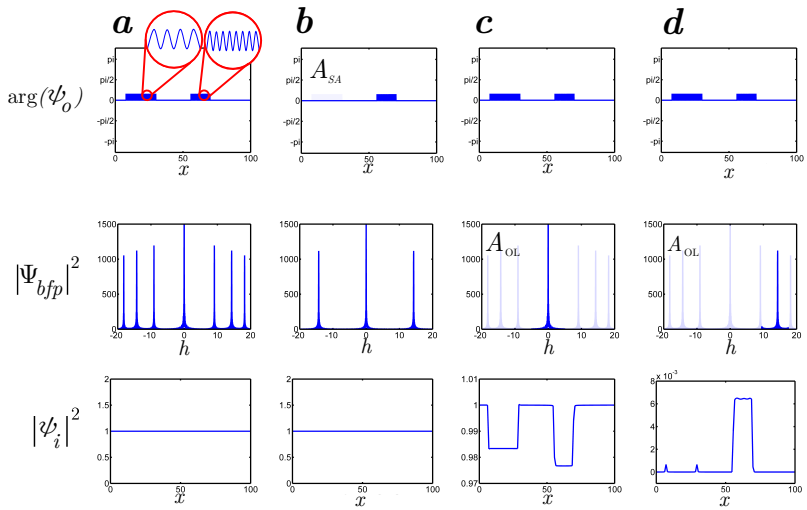

Figure 3.2: MatLab simulation of ψ in the object plane (top), back focal plane (middle) and image plane (bottom) of the objective lens. (a) A specimen consisting of two pure phase objects with different lattice parameters. A diffraction pattern can be recorded in the back focal plane but no image appears in the image plane. Pure phase objects, imaged using perfect lenses (at zero defocus), do not give rise to image contrast. (b) In SAED, only part of the specimen is allowed to contribute to the diffraction pattern. The information in the back focal plane is limited to the aperture selection. (c) Diffraction contrast can be obtained in BFTEM images when a small objective lens aperture is inserted in the back focal plane. In this case, only the central diffraction spot is allowed to pass and an image of the two phase objects appears dark on a bright background. (d) If the central diffraction spot is excluded, the phase objects are imaged as bright on a dark background. When a single spot is selected in DFTEM, only the phase object associated with that spot is bright.

Objective lens aberrations introduce changes in phase between the scattered beams and the direct beam. This phase error, $\chi(h,k)$, has many components including image shift, astigmatism and coma. The two dominant components for a properly aligned JEOL 3000F are defocus, $\chi_{df}(h,k)$, and spherical aberration, $\chi_{\mathrm{CS}}(h,k)$, hence $\chi \approx \chi_{df} + \chi_{\mathrm{CS}}$. The phase error due to spherical aberration is a fourth-order polynomial function and depends only on the acceleration voltage for a given microscope (the spherical aberration constant, $\mathrm{C_S}$, for a JEOL 3000F at 300kV is 0.6 mm). The phase error due to defocus is a second-order polynomial function which varies with defocus. Figure 3.3 shows how the phase error changes with the spatial frequency (or scattering angle).

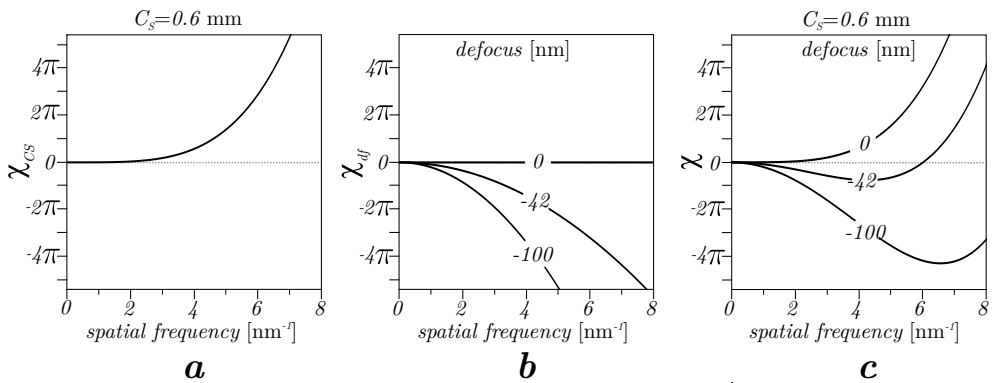

Figure 3.3: Phase change between the direct beam and the scattered beams (phase error) as a function of the spatial frequency. (a) For spherical aberration $\chi_{\mathrm{CS}}(h,k)$. (b) For defocus $\chi_{df}(h,k)$ with three different defoci: 0 nm, -42 nm and -100nm. (c) The total phase error χ. Here $\chi = \chi_{df} + \chi_{\mathrm{CS}}$.

The phase error is best introduced in our model in Fourier space, thus revising relationship 3.5 to:

$$\mathcal{F}^{-1}\left(e^{-i\chi}\, A_{\mathrm{OL}}\, \Psi_{bfp}\right) = \psi_i \tag{3.7}$$

MatLab simulations of ψ including an ideal phase error are shown in Figure 3.4, and it is clear that the phase error is a requirement for HRTEM imaging [I-VII, IX].

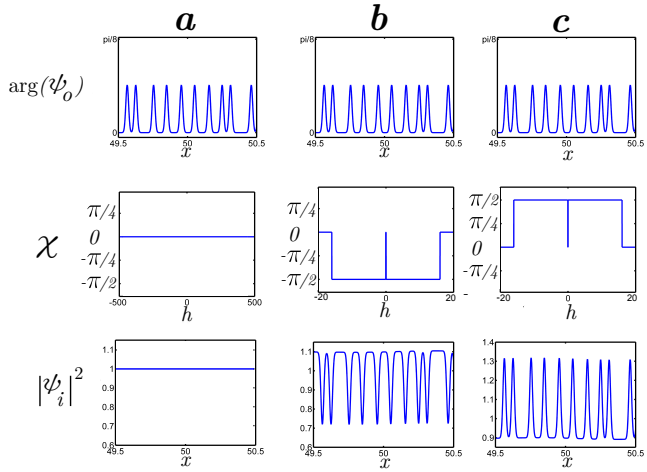

Figure 3.4: MatLab simulation of ψ in the object plane (top) and image plane (bottom) of the objective lens, and graphical representations of the phase error (middle). Note that the resolution obtained using diffraction contrast in BFTEM is too low for high-resolution imaging. (a) No image contrast appears without phase error (perfect lenses at zero defocus). (b) HRTEM imaging using an ideal negative phase error. Atoms appear dark on a bright background. (c) HRTEM imaging using an ideal positive phase error. Atoms appear bright on a dark background.

Since the image contrast, $\mathcal{C}$, is now linked to the scattering angles in the back focal plane (as a result of the phase error), the reciprocal form of the contrast, $\mathcal{F}(\mathcal{C})$, helps with image interpretation. The relationship can be made more clear using the *linear imaging approximation* which states that it is sufficient to consider interference between the direct beam and scattered beams (consequently discarding internal interference between scattered beams).[37]

$$\mathcal{F}(\mathcal{C}) \approx \left[\mathcal{C} \propto |\psi_i|^2\right] \approx \delta + V_t \; A_{\mathrm{OL}} \; 2\sin(\chi) \tag{3.8}$$

Here, δ is the Dirac delta function and $\sin(\chi)$ is called the phase contrast transfer function (pCTF). Note that sample information, V_t, is expressed differently depending on whether $\sin(\chi)$ is positive or negative. In Figure 3.5a, pCTFs for a JEOL 3000F are shown at three defoci. A defocus of -42 nm optimally balances the phase error caused by spherical aberration and the contrast is transferred similarly to the widest possible band of spatial frequencies. At high spatial frequencies, contrast transfer flips between negative and positive for small changes in spatial frequency and contrast are hard to interpret. The first crossing of the x-axis is called the *resolution limit* and an objective lens aperture is usually inserted in the back focal plane to exclude

all contributions beyond this point. Variations in the illumination and fluctuations in the lens currents and high voltage dampen the pCTF, but this effect is mainly beyond the resolution limit for a JEOL 3000F and is not shown here.

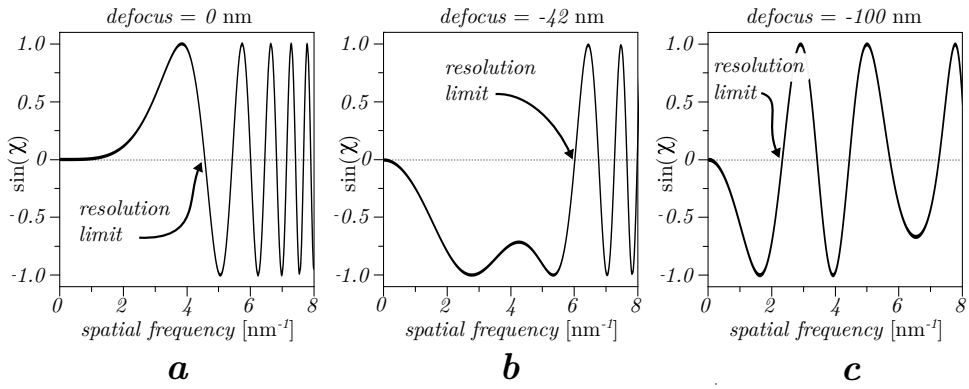

Figure 3.5: Phase contrast transfer function (pCTF) for a JEOL 3000F at different defoci. (a) At 0 nm defocus, the low frequency pCTF was positive and the *resolution limit* set the maximum point-to-point resolution to about 4.6 nm^{-1} or 0.22 nm. (b) At the optimum defocus of -42 nm, the pCTF was negative and the resolution limit was 6.0 nm^{-1}, or 0.17 nm. (c) At -100 nm defocus, the resolution limit was 2.4 nm^{-1}, or 0.42 nm

STEM and XEDS

STEM images [I-II,VII-X] are formed by plotting the intensity of a signal as a function of beam location. Image contrast is caused by variations in signal strength as the beam is scanned over the sample. Two common signals are scattered electrons and emitted X-rays.

The diffraction pattern from a convergent beam vs. a parallel beam differ in that diffraction spots grow into diffraction disks as the incident beam gets more and more convergent. The intensity in the diffraction disks can be used as an image-forming signal in STEM (see Figure 3.6a), which is known as annular dark-field (ADF) or sometimes as low-angle annular dark-field (LAADF). Using the direct beam as the image-forming signal is called bright-field (BF), while using the electrons scattered to angles outside the conventional diffraction pattern is called high-angle annular dark-field (HAADF). At these high angles (far over 30 mrad), electrons are primarily scattered by incoherent thermal diffuse interactions which are proportional to the atomic number and sample thickness, resulting in *mass/thickness contrast* in HAADF images.[38]

There is also the option to record images based on other signals than

electron intensity. The electron beam in a transmission electron microscope carries enough energy to excite inner-shell electrons. The excited or ionized atom can lower its energy by filling the empty state with an outer-shell electron, while the excess energy is carried away by an X-ray photon or an Auger electron. X-ray photon energy is measured using an energy-dispersive spectrometer and one usually plots the number of photons vs. the energy (shown in Figure 3.6b). In the X-ray energy-dispersive spectrum (XEDS or sometimes EDS or EDX)[I-II, VIII, IX-X] each element has a unique set of peaks. Peak intensities can be used for quantitative analysis giving the stoichiometry or mass ratio. Detailed analyses are, however, limited by pathological overlap and channeling effects.

The resolution in STEM images is generally dependent on probe size, but can also be affected by the type of sample and signal used. The minimal detectable fraction for any element (about 0.5–1 at%) has to be considered when interpreting XEDS element maps or quantitative data.

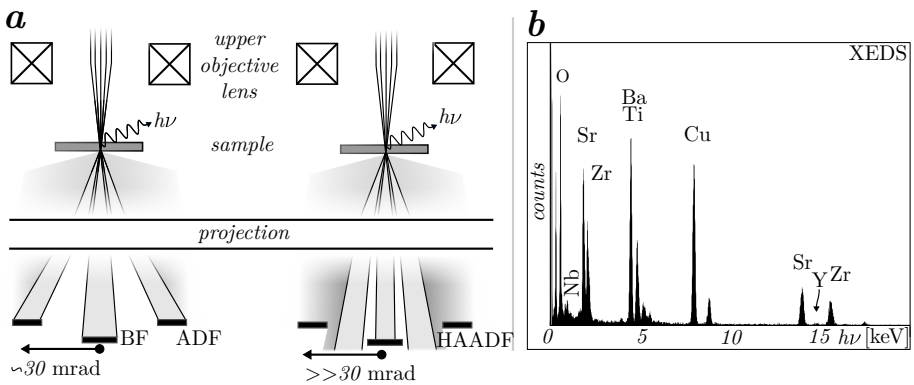

Figure 3.6: (a) Schematic ray diagrams of bright-field (BF), annular dark-field (ADF) and high-angle annular dark-field (HAADF). A focused electron beam scans over the sample and images are created using the signal from the BF or the ADF detector, which sits in a conjugate back focal plane. Lenses underneath the sample are used to set the camera length for either BF, ADF or HAADF mode. (b) A X-ray energy dispersive spectrum (XEDS) can be used for chemical analysis since each element has a unique set of peaks. However, peaks from different elements can overlap, such as Ba and Ti.

4 Sample Preparation

10 Fold???

— Dan Shechtman [39]

In materials science, sample preparation for transmission electron microscopy (TEM) usually involves making the specimens thin enough. Common (thinning) preparation techniques include mechanical crushing or polishing and (broad or focused) ion milling. Nanowires require almost no preparation since they are often electron transparent after synthesis. However, the nanowires must be broken off the substrate in order to bring them into the microscope. Examining the nanowire–substrate interface thus becomes impossible and the nanowires can only be imaged perpendicular to their growth axis. To circumvent these limitations, sample preparation must be applied to the nanowire samples. This chapter discusses two such methods. Both are based on focused ion beam (FIB) machining which has advantages over mechanical polishing and broad ion milling. These advantages include simultaneous milling and imaging, *in-situ* deposition of protective metal and site specificity.

In the literature there is confusion about the meaning of *plan view* and *cross-section* when it comes to TEM of nanowires. Some authors use plan view when describing images of nanowires viewed perpendicularly to the long axis, i.e., lying flat on a holey carbon film for example.[40–43] These authors tend to use cross-section to describe images of nanowires that are recorded parallel to the long axis. Other authors use plan view for this image direction [44–46]. It is problematic to use *cross-section of nanowire* as a reference to only one type of image direction, since many types of cross-sections can be prepared for TEM. For example, cross-sections both parallel and perpendicular to the long axis are possible, especially if the nanowire has a diameter greater than 100 nm. A cross-section can also be prepared of the nanowire–substrate interface or device components such as wrap gates. In the following text, the type of cross-section will be described as either *side view*, allowing a cross-sectional view of the substrate including the nanowire–substrate interface, or as *top view*, enabling imaging parallel to the long nanowire axis.

It is important to note that FIB thinning is damaging to the crystal structure and can alter the chemical composition of the material. The depth of the damage mainly depends on the impact angle and acceleration voltage and can be minimized to acceptable levels by polishing at a grazing angle using low voltage.[47,48] For an introduction to the FIB instrument, and to general sample preparation using FIB, the textbook by Giannuzzi and Stevie [49] is recommended.

Side view cross-section

Side-view cross-section preparation makes it possible to perform TEM with a projection parallel the to substrate surface [I, III, IV-VI]. The nanowires are seen from the side and are still attached to the substrate. An example of the use of this method is shown in Figures 4.1. Imaging can thus be performed through the substrate, interface and nanowires in $\langle \bar{1}10 \rangle$ / $\langle \bar{1}\bar{1}20 \rangle$ projection for *3C/2H* structures.

One of the difficulties with preparing side view cross-sections using FIB is the sensitivity of the nanowires. Due to their small diameter they are easily damaged by the ion beam. Nanowires that are directly struck by the ions tend to lose crystallinity and become, partly or completely, amorphous [45,50]. Nanowires that are outside the area that is exposed to ions tend to become covered in sputtered material.[36] A solution to these problems is to embed the nanowires in a material that functions as a protection without altering the sample. A protective metal, deposited using electron or ion beam-induced deposition inside the FIB instrument is a close-at-hand, but not ideal, solution. Slow sputter-etching metals on top of high aspect ratio nanowires tend to result in curtain shaped lamellae. Fresnel fringes, which occur when a heavy metal is deposited directly on the semiconductor material, can be problematic when imaging thin nanowires. Resins used in ultraviolet and electron beam lithography have proven to be suitable protection materials. The sputtering rate and electron-optical density is a better match for semiconductor nanowires. Such resins have low viscosity and can be spin coated on the substrate without trapping air bubbles or causing the nanowires to break. The manufacturers provide instructions on how to achieve precise thicknesses, simplifying the adaption of the method for different nanowire lengths. During soft bake on a hot plate the resin hardens slowly without much movement, keeping the nanowires in their upright position. After soft bake, the water content in the resin is low enough not to cause problems for the vacuum system in the FIB instrument. When embedded in resin, the nanowires can be prepared for side view cross-section by following standard lift-out procedures, as described in e.g., [51].

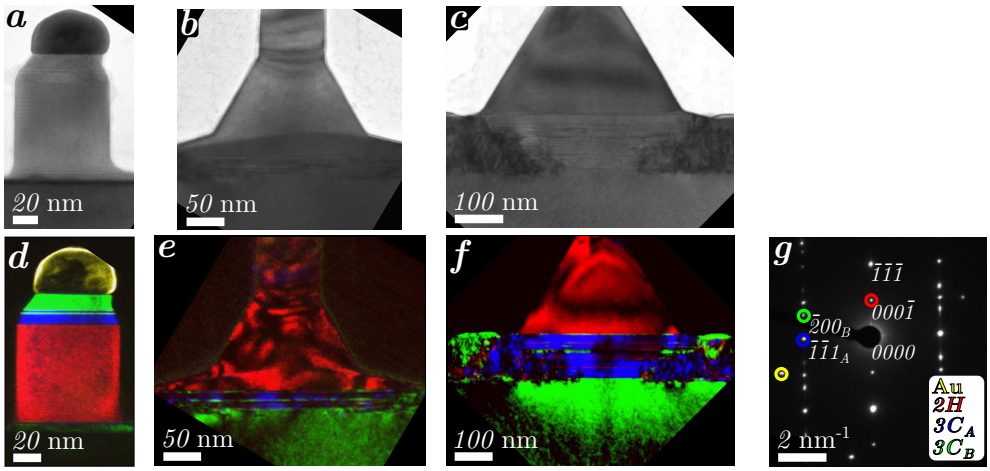

Figure 4.1: The evolution of the interface structure in GaAs nanowires seen in $[\bar{1}\bar{1}20]$ (*2H*), $[\bar{1}10]$ ($3C_A$) and $[01\bar{1}]$ ($3C_B$) projection [III]. (a)-(c) BFTEM images of nanowires where the synthesis was stopped after 30 s (a), after 240 s (b) and after 270 s (c). (d)-(f) Corresponding DFTEM images where *2H* structure is seen in red and *3C* in green and blue, where green and blue correspond to different twin orientations. (g) A typical diffraction pattern with the diffraction spots used for DFTEM labeled. Note that the forbidden 0001 spot is seen here due to double diffraction. The nanowires have been prepared for TEM using the side view cross-section FIB method.

The FIB-based side view cross-section preparation method is useful in a variety of scenarios. For example when: 1) specific sites on a substrate or individual nanowires need to be hand-picked for TEM analysis. This is often the case when the samples have been previously analyzed with other techniques such as scanning electron microscopy or cathode luminescence. Nanowires for which such complementary techniques have led to the discovery of interesting characteristics can be selected and prepared for TEM analysis. 2) Entire devices can be prepared for TEM, including nanowires, contacts, substrate and buffer layers. All parts thinned to similar thicknesses, and pre-oriented in a useful crystal orientation. 3) Nanowire-based structures that are too thick for TEM can be thinned down to electron transparency. Such nanowires are often radial heterostructures of the type *core/multi-shell*, where the thinning process removes shell material that would otherwise overlap in the TEM projection. The interfaces between the shell-layers and core are imaged edge-on.

Top view cross-section

Nanowires are usually a few μm long, making TEM with a projection parallel to the growth direction impossible. In this viewing direction nanowires are simply not electron transparent. Top view cross-section preparation removes most of the nanowire while keeping a short, electron transparent segment [I]. A typical image direction is thus $\langle 111 \rangle$ / $\langle 0001 \rangle$ for *3C*/*2H* structures.

One of the difficulties when preparing a top-view cross-section using FIB is that the substrate is removed leaving the nanowire segments without any support. If the nanowires are toppled over on to their side, the growth substrate can be used as support. But this technique is rarely suitable for more than one to three nanowires per lamella [41, 52, 53]. Another solution is to embed the nanowires in a supporting medium and lift out a lamella parallel to the substrate surface (consequently perpendicular to the normal growth direction). Spurr's epoxy [54] has proven suitable as an embedding material since it has low viscosity in its pre-hardened state and can flow in between the nanowires. In its hardened state it supports the nanowire segments without evaporating or deforming. Even so, the lamella might still bend or warp. A frame lamella design can give extra support [55–57]. The idea of the frame design is that certain sections of the lamella are left thick to provide support to the thin region of interest (ROI). An example of a frame lamella can be seen in Figur 7 on page 66.

In Figure 4.2, the steps for preparing a top view cross-section of nanowires in a frame lamella are shown. A summary comprising eight steps is given below. 1) Place the nanowire sample in a mold and cast the entirety in Spurr's epoxy. 2) Polish one side of the hardened epoxy tablet mechanically until a side facet of the substrate is exposed (Figure 4.2b-c). 3) Cover the tablet in a thin layer of conducting material to avoid charging in the FIB instrument. 4) Find the region with nanowires where the epoxy meets the exposed substrate. 5) Lift out a lamella (parallel to the substrate surface) that is thick enough to include the nanowires plus about 1 μm of substrate material. 6) Do not polish the entire lamella but only the ROI. 7) When polishing the substrate side, leave a crossbar of substrate material running parallel to the ROI (notice that the crossbar might overlap parts of the ROI in TEM). 8) Thin the ROI to electron transparency. The ROI should be attached to thick sections of the lamella on two sides, and the thick sections should be connected by the crossbar, as in Figure 4.2d(8).

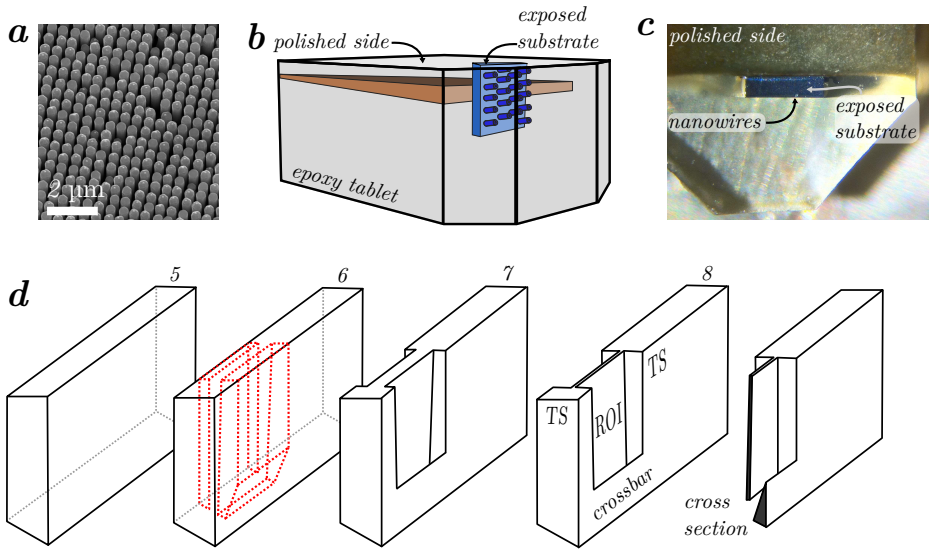

Figure 4.2: The preparation process of a top-view cross-section for nanowires [I]. (a) Scanning electron microscopy image of the nanowires before any preparation [courtesy of Daniel Jacobsson]. (b) Schematic illustration of the sample, mounted on a piece of cardboard for support, casted in epoxy. (c) Photo of the polished side of the epoxy tablet. (d) Frame lamella preparation where the numbers correspond to the steps mentioned in the text. TS is the abbreviation for thick section and ROI for region of interest.

The FIB-based top view cross-section preparation method is useful for imaging nanowires in the, usually unobtainable, growth direction as is shown in Figure 4.3. In this projection there are no channeling effects distorting X-ray energy-dispersive and electron energy loss spectroscopy. The different segments in core/shell heterostructures and many of the nanowire side facets are imaged edge on. Internal chemical and structural features, such as Al segregation, are detectable [40, 44, 53].

Cross-sections from a fixed segment on the nanowires are prepared using the substrate as a point of reference. If the lamella is prepared at an angle to the substrate [58], the cross-sections from adjacent nanowires will come from slightly different locations, as shown in Figure 4.4. At one end of the lamella, the cross-sections are cut close to the substrate while at the opposite end of the lamella the cross-sections are cut at the very top of the nanowires, with a gradient of positions between. An example of an angled lamella can be seen in Figur 5 on page 63. This makes it possible to follow general structural and chemical trends along the growth direction while imaging in $\langle 111 \rangle$ / $\langle 0001 \rangle$.

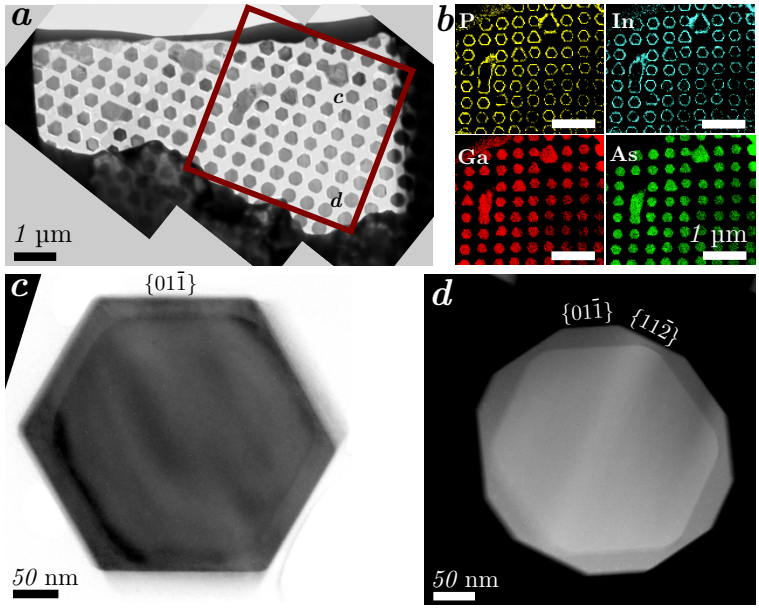

Figure 4.3: Top-view cross-section of GaAs/$Ga_xIn_{1-x}P$ core/shell nanowires [I]. (a) TEM overview image of the lamella. (b) XEDS element maps of the square area marked in (a). (c)-(d) Change of the shell faceting along the nanowires. Close to the top, only $\{01\bar{1}\}$ type facets are observed while closer to the substrate the shell has both $\{01\bar{1}\}$ and $\{11\bar{2}\}$ type facets. The nanowire labeled *c* in (a) is seen in (c) as a TEM image and the nanowire labeled *d* in (a) is seen in (d) as a STEM image.

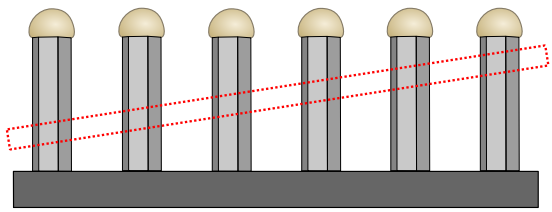

Figure 4.4: Lamella for top-view cross-section of nanowires with an angle relative to the substrate surface. Adjacent nanowires are cut at slightly different positions, progressively from the substrate to the top.

5 Crystal Twinning

Hold on... What exactly is this thing?

— Genpei Akasegawa [59]

Semiconductor materials in the (Al, Ga, In)N system typically have the *2H* crystal structure, although *3C* can be stabilized [60, 61]. Semiconductor materials in the (Al, Ga, In)(P, As, Sb) system typically have the *3C* crystal structure in bulk, but can in nanowires also exhibit *2H* and *4H* [62, 63]. This polytypic crystal structure phenomenon is due to the high surface-to-volume ratio of nanowires, where the side facet surface energy is important [64, 65].

Nanowires from both systems, collectively known as III–V semiconductors, often grow in a ⟨111⟩ / ⟨0001⟩ crystal direction, which is assumed here unless stated otherwise. III–V materials are polar in the ⟨111⟩ / ⟨0001⟩ direction (as illustrated in Figure 2.3b) and the growth results are different in the two directions. N, P or As-terminated surfaces, called V-polar, are often used for (Al, Ga, In)(P, As, Sb) nanowires [66, 67] while Al, Ga or In-terminated, or III-polar, surfaces are frequently used for (Al, Ga, In)N nanowires [IV]. The III-polar and V-polar surfaces are sometimes referred to as {111}A / {0001}A and {111}B / {0001}B, respectively. Nanowires with a V-polar growth front are usually defined to grow in the $[\bar{1}\bar{1}\bar{1}]$ / $[000\bar{1}]$ direction.

Stacking faults in these systems are simply alternatives to the stacking sequence of the a, b and c-layers discussed in Chapter 2 (see Figure 2.1). For instance, if the sequence is $...abc\hat{a}cba...$ this can be seen as two mirrored *3C* sequences, meeting at an a-layer (hat, $\wedge$, marks the mirror plane, or contact plane). Even though the stacking sequence is mirrored, this is not necessarily the case for the crystal structure, since each layer is actually a bilayer with two types of atoms. Using the same notation as in the GaAs example in Chapter 2, with As layers as superscript on the Ga layers, the same mirrored sequence becomes $...a^{b}\, b^{c}\, c^{a}\, \hat{a}^{c}\, c^{b}\, b^{a}\, a^{c}...$ which is in fact not mirrored.

Another way to describe this phenomenon is as crystal twinning. The twin (symmetry) operation is in this case a 60° rotation around a common ⟨111⟩ axis with a {111} contact plane, as illustrated in Figure 5.1. Since all bonds in the contact plane are heteroatomic (Ga–As), it is sometimes referred to as an ortho twin. If both the stacking sequence and crystal structure were

mirrored, homoatomic bonds (e.g. As–As) would be present at the interface and the result would be a para twin. Stacking sequences in para twins are $...a^b\ b^c\ c^{a\sim a}c\ \ ^cb\ \ ^ba...$ (para-As twin) or $...^ca\ \ ^ab\ \ ^b\hat{c}c^b\ \ b^a\ \ a^c...$ (para-Ga twin).[68, 69] Para twins are less likely to occur due the formation energy being higher than for ortho twins.[65, 70, 71] Para twinning would invert the polarity in nanowires which have only been observed in the (Al, Ga, In)N system where it was believed that impurity atoms had migrated to the inversion interface, thus eliminating the need for homoatomic bonds [72]. The following text will assume ortho twinning.

Inclined twins in *3C*

Since the *3C* structure has cubic symmetry, there are 4 equivalent {111} contact planes where ortho twinning can occur. In nanowires, however, the presence of a growth direction sets twinning with rotation around the [111]/[$\bar{1}\bar{1}\bar{1}$] axis in a special category. Such twins, with rotation around the growth axis, are here called perpendicular twins (PT), illustrated in Figure 5.1a. Twins with rotation around another ⟨111⟩ axis are here called inclined twins (IT), illustrated in Figure 5.1b-c.

The formation of inclined twins during nanowire synthesis can have major impacts on the morphology since this can cause a kink in the nanowire.[67, 73, II] When using a closed cell for *in-situ* transmission electron microscopy (TEM) nanowire growth experiments, such a kinking event was captured on video (15 frames per second). Six still images from the video are shown in Figure 5.2. The video recording was started soon after extra source material had been provided to a growing InAs nanowire. The growth was assumed to be in V-polar [$\bar{1}\bar{1}\bar{1}$] direction since all inspected nanowires from that and similar experiments were V-polar. The sudden influx of material made the Au seed particle expand from 52 to 55 nm due to In uptake (according to the vapor–liquid–solid growth model, it is only the group 13 element (Al, Ga, In) that dissolves into the catalyst particle [74, 75], with the exception of Sb [67]). As the particle expanded, an inclined twin formed, marked by an arrow in the 0 s panel. The situation resembles the one in Figure 5.1b. In less then 30 s, a second inclined twin formed, marked in panel 29.3 s (resembling the situation in Figure 5.1c). This resulted in an inclined segment with a different crystal orientation as opposed to the main nanowire, shown as green in Figure 5.2. After about 50 s of continued growth, the first twin interface reached the side facet, marked by an arrow in panel 51.0 s. Growth rates differed between the types of InAs surfaces that were in contact with the Au particle. New material

was added unevenly over the growth front and the particle changed growth direction, pivoting around the point at the side facet. This continued until a new V-polar surface came in contact with the Au particle after about 130° of rotation, and the nanowire could continue its growth.

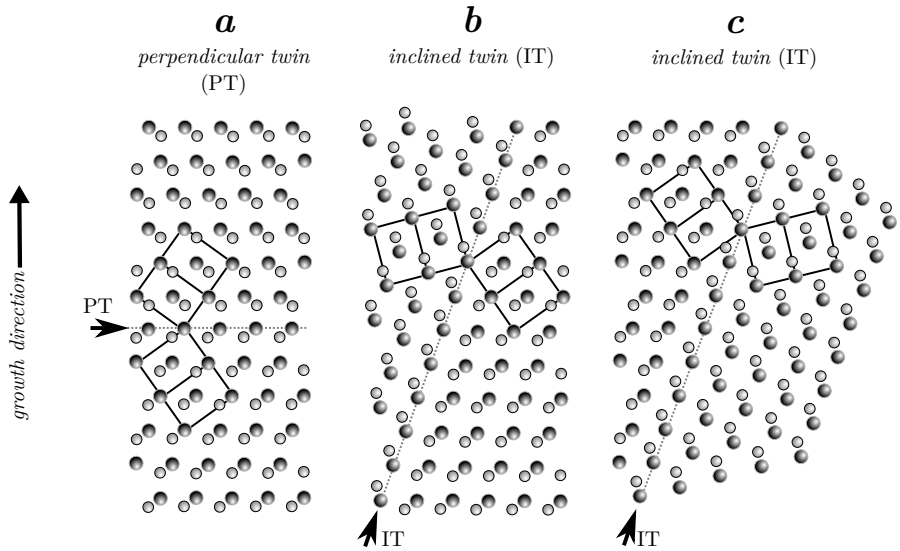

Figure 5.1: Projection models of twins in *3C* nanowires seen along a $\langle \bar{1}10 \rangle$ axis with unit cells in black lines. The twin operation involved a 60° (or 180°) rotation around a common $\langle 111 \rangle$ axis, and the contact plane was $\{111\}$. (a) A perpendicular twin (PT) where the nanowire growth front remained V-polar after twin formation. (b) An inclined twin (IT) where the growth front changed from V-polar to III-polar. (c) An inclined twin where the growth front changed from III-polar to V-polar.

About half of the investigated nanowires synthesized in the closed cell had inclined twins in the earliest segments formed, i.e. in the end opposite to the Au particle after synthesis. A few examples are shown in Figure 5.3 where one inclined twin and one perpendicular twin are marked in each nanowire. An important difference between these nanowires and those synthesised using more common methods was the substrate. Normally, seed particles are placed on a crystalline substrate where the nanowires form an epitaxial interface and adopt the polarity of the substrate [67, 76, 77]. In the closed cell experiment, however, the seed particles were placed on an amorphous carbon film and could neither form a coherent interface nor adopt a given polarity.

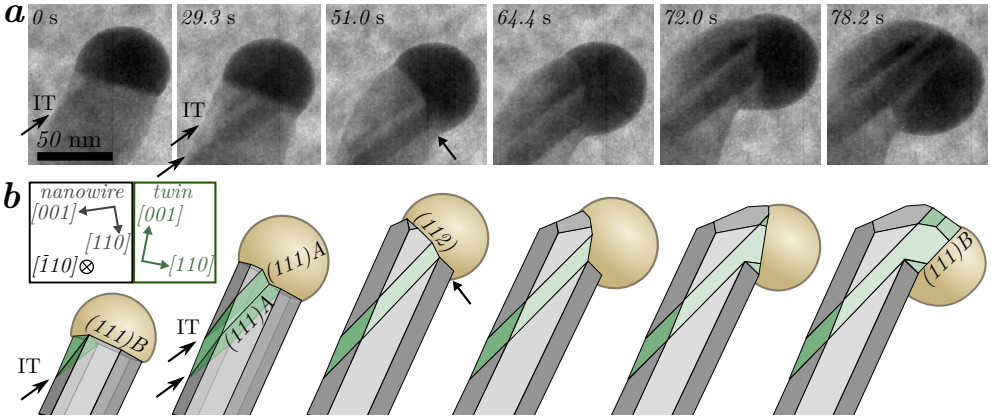

Figure 5.2: Images and models of an Au seeded InAs nanowire under a kinking event [II]. (a) Time-lapse TEM images recorded over a period of 80 s. The nanowire was imaged approximately 10° from a ⟨110⟩ zone axis, making the twin crystal visible between dark bands of overlapping {111} twin planes (arrows in the 0 s and 29.3 s panels). The arrow in panel 51.0 s indicates the pinned growth front. (b) Corresponding models to the images in (a). The 51.0 s model and onwards are shown in ⟨110⟩ projection to better illustrate the facets.

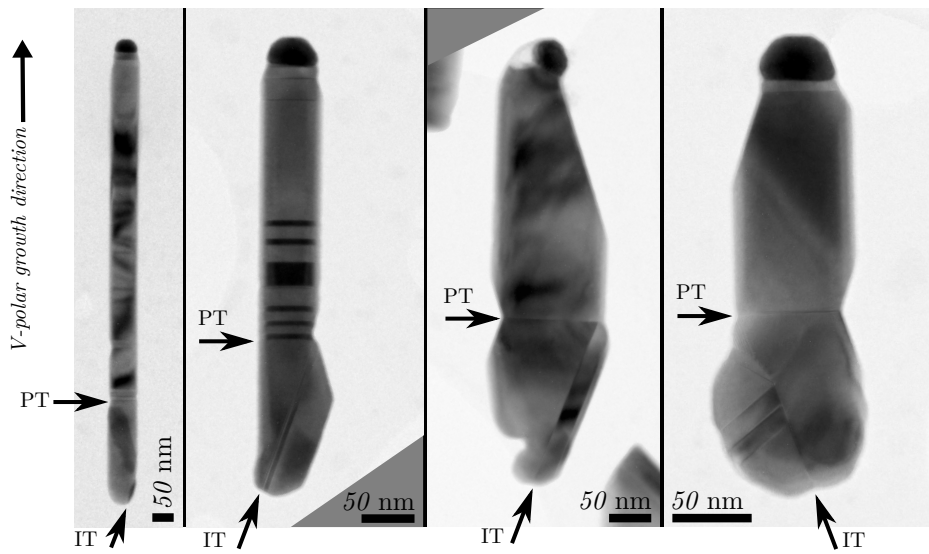

Figure 5.3: Inclined (IT) and perpendicular twins (PT) in InAs nanowires synthesised without crystalline support [II]. All nanowires have been determined to grow in the V-polar [$\bar{1}\bar{1}\bar{1}$] direction using convergent beam electron diffraction.

Nanowires synthesized in the gas phase without any substrate also exhibited early inclined twins [78], indicating that the twin interface might be functional during nanowire synthesis. A speculative account of the events is that the original growth direction was $\langle \bar{1}\bar{1}\bar{2} \rangle$, along the twin contact plane, since the twin interface stabilized the growth. One of the twin crystals will have a slower-growing III-polar surface while the other will have a faster-growing V-polar (as in Figure 5.1c). The V-polar twin crystal will eventually dominate and shift the growth direction to $\langle \bar{1}\bar{1}\bar{1} \rangle$, as for all of the nanowires in Figure 5.3.

Lateral twins in *3C*

A twin with the same twin operation as the perpendicular and inclined twins, but a different contact plane is schematically illustrated in Figure 5.4. In the figure, the structure contains two perpendicular twins that partly penetrate the crystal. These two partial twin interfaces are separated by nine {111} layers in the nanowire growth direction, leading to the formation of a lateral twin (LT) with a $\{11\bar{2}\}$ contact plane. (In the observed structure, the twin interface was about 200 nm long, or approx. 600 {111} layers.) The mirrored structures were point-matched every three layers and shared a V-polar $[\bar{1}\bar{1}\bar{1}]$ axis [79, 80]. This twin is often referred to as $\Sigma = 3$ $\{11\bar{2}\}$, where Σ is the reciprocal density of coincidence sites [81]. The interface in the lateral twin deviates from a perfect crystal structure and the physical properties are expected to be dissimilar to that of the bulk material.[82] The perpendicular and inclined twins mentioned earlier, on the other hand, have an overall atomic structure that is very close to the perfect crystal structure.

The observation was made in a sample of radially merged nanowires where HRTEM images (not shown here) and SAED patterns were recorded in a $\langle 110 \rangle$ zone axis that was 60° from the axis parallel to the contact plane (rotation around the nanowire growth axis). The regions of interest and diffraction patterns are shown in Figure 5.5 and an overview of the sample is displayed in Figure 5.8a. The SAED pattern from a region including a perpendicular twin have diffraction spots from both twin crystals (Figure 5.5b). The diffraction pattern recorded through the lateral twin $\{11\bar{2}\}$ interface additionally included double diffraction spots (Figure 5.5c).[83, 84] One route to form the $1/3(111)$ double diffraction spots is shown in Figure 5.6. SAED from inclined twins can produce similar patterns when recorded in a direction that is not parallel to the contact plane. Such patterns do not, however, have double diffraction spots along the nanowire growth direction. This is because the $\langle 111 \rangle$ direction is shared by an inclined twin and the main nanowire is not in the growth direction.

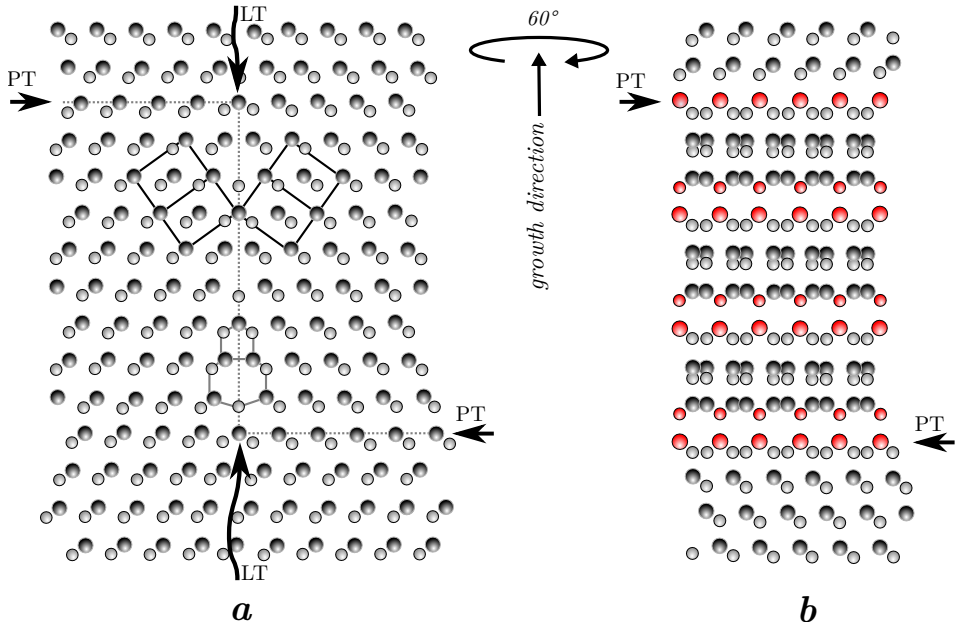

Figure 5.4: Projection models of a lateral twin (LT) in *3C* nanowires seen along a ⟨110⟩ axis with unit cells in black lines. The twin operation was a 60° (or 180°) rotation around a common ⟨111⟩ axis, and the contact plane was $\{11\bar{2}\}$ (parallel to the growth direction). (a) Projection through a ⟨110⟩ zone axis parallel to the contact plane. Every third layer in the growth direction were lined up. (b) Projection through a ⟨110⟩ zone axis that was 60° from the one in (a) (rotation around the nanowire growth axis). The periodicity along the growth direction was extended by three:
...c a b c a b c a b c a b ĉ b a...
...c a b ĉ b a c b a c b a c b a...

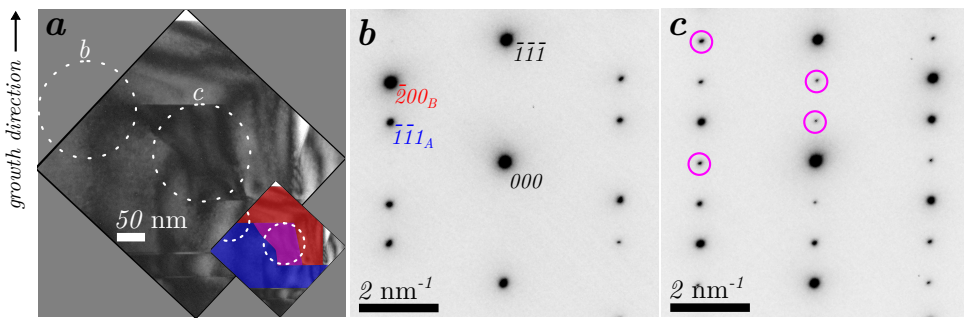

Figure 5.5: Lateral and perpendicular twins in radially merged GaAs nanowires. (a) Regions of interests with the positions of the selected area aperture, marked with white circles. The inset is a colored version of the image where one twin orientation was colored red, the other orientation was colored blue and the overlap was colored purple. (b) $3C_A$ $[\bar{1}10]$ and $3C_B$ $[01\bar{1}]$ direction SAED pattern including both sides of a perpendicular twin plane. (c) $3C_A$ $[\bar{1}10]$ and $3C_B$ $[01\bar{1}]$ direction SAED pattern of the twin crystals through the lateral twin $\{11\bar{2}\}$ interface. Double diffraction spots were visible at a 1/3 and 2/3 distance between the 000 and $\bar{1}\bar{1}\bar{1}$/111 spots.

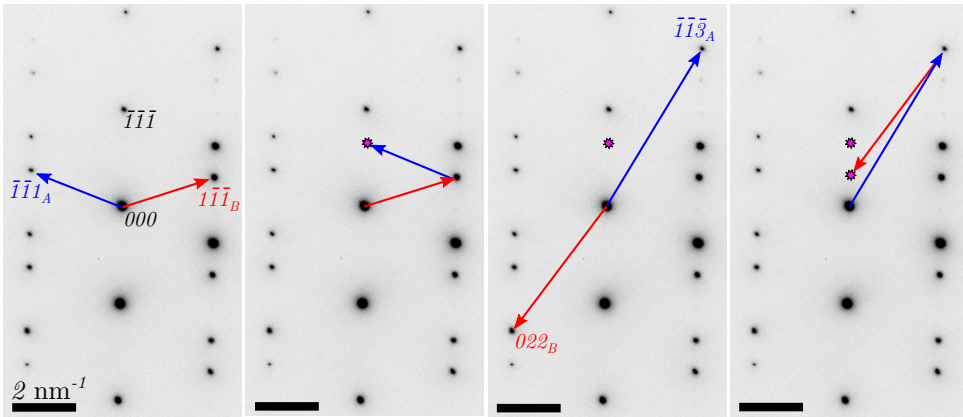

Figure 5.6: Double diffraction spot formation. The overlap of two *3C* crystals with a relative rotation of 60° created additional spots, particularly the 1/3 111 spots. Lateral twins (LT) can, in nanowires, be distinguished from inclined twins since the double diffraction spots appear in the growth direction. They can also be distinguished from perpendicular twins if the SAED is recorded perpendicular to the growth axis.

Perpendicular twins in *2H* and *3C*

Crystal structure transformation from *2H* to *3C* can be induced in nanowires by, for example, burying the nanowire in a bulk material [85] or by heating the nanowire using an electron beam [86]. Radially merging *2H* nanowires is another way that also introduces interesting features. Figure 5.7 shows the outcome after two *2H* GaAs nanowires were grown thicker and thicker until their side facets met. Initially the nanowires were grown as thin *2H* structures, but during a second step in the synthesis, new material was added to the nanowire side facets as well as to the substrate surface. The growth on the substrate was *3C*-structured with a high twin density, while the radial growth on the nanowires continued in *2H*, until coming into physical contact with another structure. In the case imaged in Figure 5.7, only about 1 µm of the nanowires, from the substrate and up, were in contact and displayed a changed crystal structure. The remaining top segments maintained their original *2H* crystal structure (blue in Figure 5.7b). Substrate growth formed a barrier between the nanowires, keeping them from merging until about 400 nm above the substrate. On either side of this barrier, the two nanowires had their own unique pattern corresponding to a perpendicular twinned *3C* structure. Above the 400-nm mark, both (now merged) nanowires had a mutual pattern made up of a perpendicularly twinned *3C* structure.

Any part of *2H* GaAs nanowires that comes into physical contact with either substrate growth or other nanowires transforms the crystal structure to a perpendicular twinned *3C*. Transformation caused by substrate growth can also be observed in Figure 4.1 which includes images of *2H* nanowires early in the synthesis. Figure 4.1a shows the result of a synthesis that was stopped after 30 s. The typical pyramidal base had not yet formed and substrate growth was minimal. At the interface between the nanowire and substrate, 5 nm of *3C* was detected. The nanowire apparently did not start growth in *2H*, but adopted the substrate's *3C* crystal structure. The switch to *2H* occurred in the first few nanometers of growth. In Figure 4.1b, the synthesis was stopped after 240 s and here the pyramidal base, with its *2H* structure, had already formed. After 270 s of synthesis, shown in Figure 4.1c, the part of the pyramidal base that was buried by substrate growth had transformed into *3C*.

If there is no contact between nanowire and substrate, but rather between two nanowires, the transformed structure will be identical across both nanowires. As the nanowires first meet, both of them have a *2H* structure (...*ababab*...) and if the layers line up perfectly one could imagine that they would simply merge into one united *2H* structure. If the layers do not line up, for instance if one starts with *ababab*... and the other with *bababa*..., something else takes place. When the bottom *a*-layer in one nanowire comes into contact with the bottom *b*-layer in the other, the lattice sites do not match and a dislocation is formed. The dislocation can either stay at the interface or it can propagate through one of the nanowires. Such a gliding process has three translation vectors in $1/3\,[1010]$, $1/3\,[1100]$ and $1/3\,[0110]$ and estimates based on the growth temperature indicate that the propagation is not kinetically hindered. It is not yet known if one nanowire dominates over the other or if a type of layer-by-layer tug-of-war occurs between the two. The direction of the dislocation gliding process might be influenced by the type of facet being formed, i.e., longer stretches of one facet would be more energetically favorable than an unordered switching back and forth.

Another example is displayed in Figure 5.8, showing at least three partially merged nanowires. All three had slightly different leaning angles (in other words, the nanowires had non-parallel growth directions), making this a much more complicated system. Bands of *2H* and *4H* structures were found running through two nanowires. This indicates that not only perpendicular twinned *3C* could be formed by merging nanowires, but also *2H* and the unusual *4H* structure.

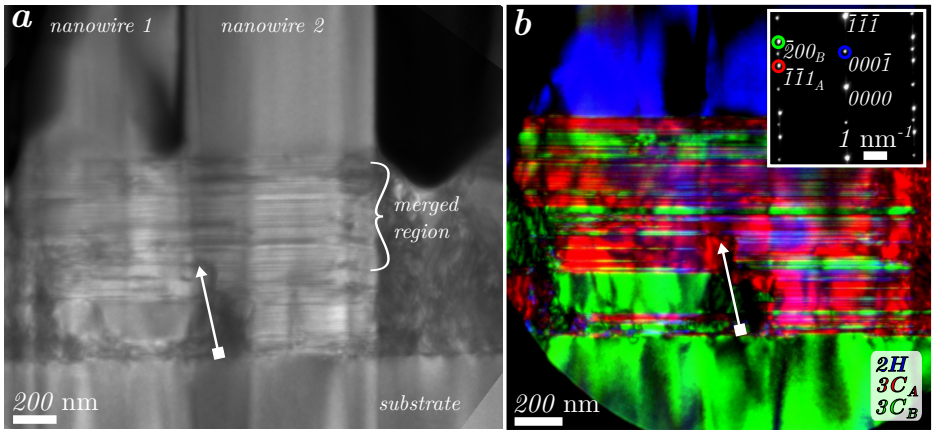

Figure 5.7: Two partially merged *2H* GaAs nanowires [III]. BFTEM image (a) and DFTEM images (b) of the substrate, transformed/merged region and the two free-standing nanowires. The arrow indicates where substrate growth hindered the two nanowires from merging. Above the arrow the two merged nanowires shared a perpendicular twinned *3C* crystal structure, up to the point where the nanowires no longer touched and exhibited their original *2H* structure. The inset shows a SAED (*2H* $[\bar{1}\bar{1}20]$, $3C_A$ $[\bar{1}10]$ and $3C_B$ $[01\bar{1}]$) pattern recorded from the area in (b) with a corresponding color coding. Note that the forbidden 0001 spot is available here due to double diffraction.

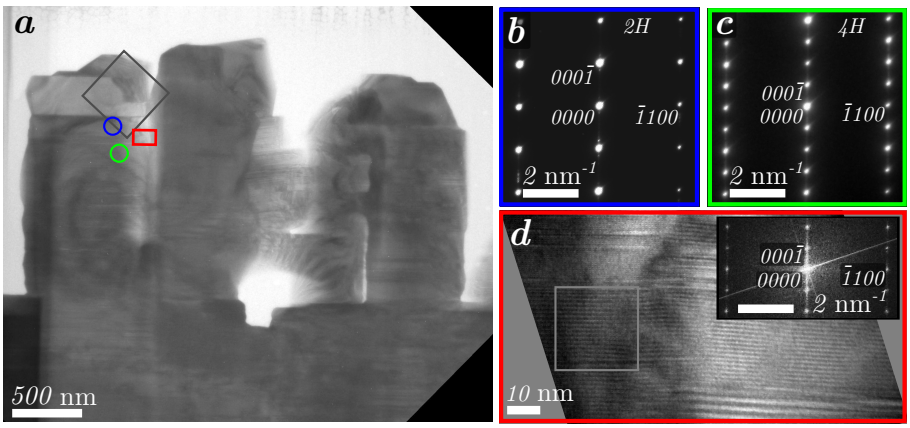

Figure 5.8: Merged GaAs nanowires where, in addition to *3C*, also *2H* and *4H* crystal structures were found in the merged region [III]. (a) Overview of the sample with three merged nanowires, BFTEM image. The square marks the region of interest in Figure 5.5a. (b)-(c) *2H* and *4H* SAED patterns from the regions marked with a blue and green circle in (a). Note that the forbidden 0001 spot is seen here due to double diffraction. (d) HRTEM image from the region marked by a red rectangle in (a) showing a band of *4H* crystal structure running across two nanowires. The inset is a Fourier transform of the gray square in the image. *2H* $[\bar{1}\bar{1}20]$ and *4H* $[\bar{1}\bar{1}20]$.

Intergrowth twins in *2H*

An unusual intergrowth twin (IGT) was observed in GaN/$Al_{0.5}Ga_{0.5}N$ radial heterostructured nanowires. The twin operation was a 90° rotation around a common $\langle\bar{1}\bar{1}20\rangle$ axis and the contact plane was $\{0001\}/\{\bar{1}100\}$, which is often referred to as a *c*-plane / *m*-plane. The nanowires are assumed to have grown in III-polar direction as a III-polar substrate was used [72,87]. The core was GaN, the shell was $Al_{0.5}Ga_{0.5}N$, one contact plane had formed between GaN and $Al_{0.5}Ga_{0.5}N$ (between core and shell) and one contact plane had formed between two $Al_{0.5}Ga_{0.5}N$ crystals (two shell segments), as can be seen in Figure 5.9. The intergrowth had first formed on the main nanowire, where an *m*-facet was used as the substrate, and grown outwards. As material also grew directly on the Si_3N_4 mask the distance between the intergrowth and the mask had increased with time. The polarity of the intergrowth twin could not be determined. Projection models of the twin are shown in Figure 5.10 with a V-polar version in 5.10a and a III-polar version in 5.10b.

The atomic arrangements at the interface between the main nanowire and this intergrowth is not yet understood. There are three major differences between the surfaces that need to be overcome to form an interface: 1) The *m*-facet is non-polar whereas the *c*-facet is polar. This means that there is either a combination of homo- and heteroatomic bonds, or an atomic arrangement very unlike the bulk. Impurity atoms might also be present, as in the case of the polarity inversion mentioned earlier [72]. 2) The bonds between *c*-planes are aligned parallel to the $\langle 0001\rangle$ axis while the bond between *m*-planes are tilted at an angle from the $\langle\bar{1}100\rangle$ axis. This implies that there will be some strain at the interface since the atoms must be torqued from their bulk positions to form bonds over the contact plane. 3) The bonds between *c*-planes are arranged in a hexagonal pattern while the bonds between *m*-planes are arranged in a rectangular pattern. The atomic arrangement at the interface must fit both the hexagonal and the rectangular symmetry and also smoothly transform from one to the other.

However, both the *c*-planes and the *m*-planes can be seen as bilayers. From this point of view the main difference between the two surfaces meeting at the contact plane is that the hexagons on the (0001)-surface are in the chair conformation while the hexagons on the $(\bar{1}100)$-surface are in the boat conformation. By including a flat *bilayer* of regular hexagons between the two surfaces the switch from chair to boat conformation is possible.

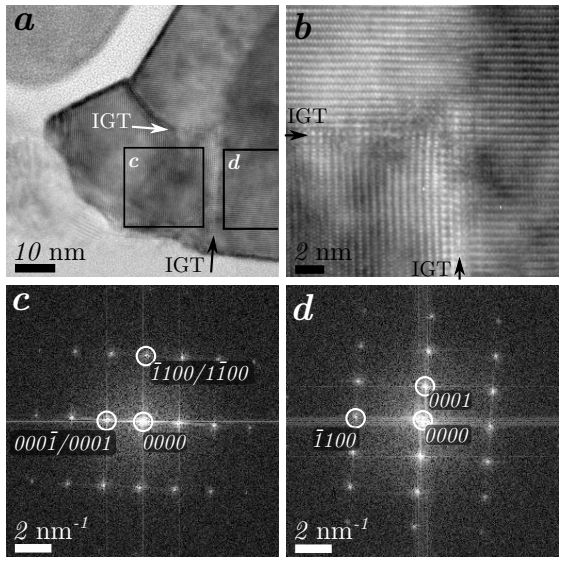

Figure 5.9: Intergrowth twin (IGT) in *2H* $GaN/Al_{0.5}Ga_{0.5}N$ radial heterostructured nanowires. (a) Overview image where the twin interfaces are marked by arrows. The growth directions of the intergrowth could be determined as it grew on an increasingly thickening substrate. (b) The region where the two interfaces met, imaged by HRTEM in $[\bar{1}\bar{1}20]$. $Al_{0.5}Ga_{0.5}N$ is on the left-hand side of the image, and GaN is on the right. (c)-(d) FFT of the squares labeled in (a). The error from a perfect 90° rotation was approx. 1°.

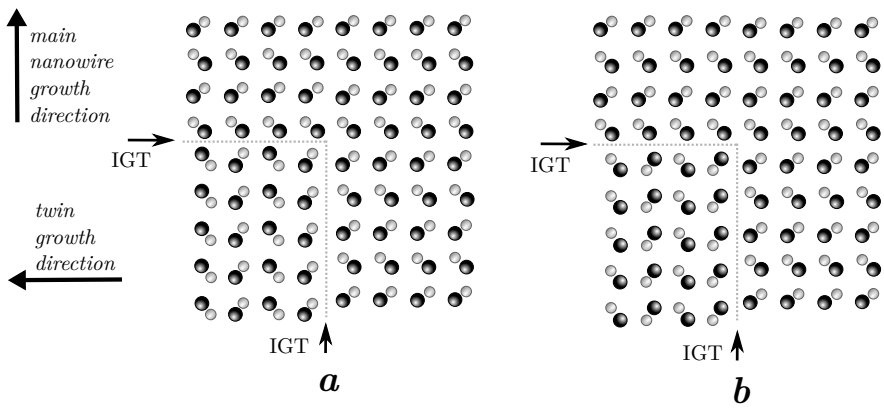

Figure 5.10: Projection models of intergrowth twins (IGTs) in *2H*. The twin operation was a 90° rotation around a common $\langle\bar{1}\bar{1}20\rangle$ axis and the contact plane was $\{0001\}/\{\bar{1}100\}$, or *c*-plane / *m*-plane. Both the growth direction and the polarity was known for the main nanowire, while only the growth direction was only known for the intergrowth twin. A V-polar model in (a) and a III-polar model in (b). There was no obvious way to model a coherent interface between the two crystals, as there was no match between atom types, positions or bonding angles.

6 Secondary Phases

That's funny!

— Alexander Fleming [88]

In solid oxide fuel cell materials, the activation energy associated with proton conduction is lower than the activation energy associated with oxygen ion conduction.[31,89,90] This means that the proton-conducting solid oxide fuel cells (PC-SOFCs) and electrolyzer cells (PC-SOECs) should be able to operate at lower temperatures (at about 250-600°C) than their oxygen ion-conducting counterparts (>600°C).[91] A low operation temperature also means that low fabrication temperatures can be used, and a wider variety of materials becomes compatible in the device. Interface reactions between different phases in these devices always constitute a risk and secondary phases can reduce the efficiency. Investigation of composition and interdiffusion can be well performed by transmission electron microscopy (TEM), and this chapter discusses the strengths and weaknesses of a few such methods.

One should note that TEM generally provides compositional information in the form of 2D images, even when the sample is thick enough to be considered a volume. This becomes a problem in cases where the phase boundary is not imaged edge-on and overlap is mistaken for interdiffusion. TEM tomography [92] and optical sectioning using an aberration-corrected scanning transmission electron microscope [93] provides 3D information, thus potentially solving the problem. But due to special requirements on samples and hardware, these techniques are not frequently used. Another solution is to prepare thin, large-area samples where the chance of finding phase boundaries aligned with the beam is greater.

Using XEDS to observe secondary phases

One way to observe interdiffusion, or the lack thereof, is to map out the elements present in the sample. If elements that should be unique to the different phases overlap the interface, interdiffusion has likely occurred. Scanning transmission electron microscopy (STEM) coupled with X-ray energy-dispersive spectroscopy (XEDS) provides a data cube of the sample where every image

pixel contains a full X-ray spectrum. A qualitative distribution map of the elements in the sample can be achieved by counting the X-ray photons at the element-specific energies. This method was used for the example shown in Figure 6.1. A test cell where a proton-conducting material with the approximate formula $La_{28-x}W_{4+x}O_{54}$ (where x refers to the solubility of W in certain La-sites) was placed on top of a Pt contact on amorphous SiO_2. The porous film of $La_{28-x}W_{4+x}O_{54}$ was synthesized using chemical solution deposition (CSD) spray coating (or spray pyrolysis), which gave rise to a porous film.

$La_{28-x}W_{4+x}O_{54}$ does not have the perovskite crystal structure described in Chapter 2, but rather requires a more complex description. Models of average structures are often given using face-centered or primitive cubic symmetry and a cell parameter of around 1.1 nm. The disorder on both the O and La sub-lattices renders a simpler description impossible. Below temperatures of about 600°C, $La_{28-x}W_{4+x}O_{54}$ behaves as a pure proton conductor and is suitable as an electrolyte in PC-SOFCs. At about 1000°C it is a mixed proton-electron conductor, comparable to the best-performing mixed proton-electron conducting perovskites, appropriate for use in dense hydrogen gas separation membranes.[94] (Many Ni-based ceramic/metal composite hydrogen electrode materials are not compatible with $La_{28-x}W_{4+x}O_{54}$ when standard processing is used. This is due to the reaction between $La_{28-x}W_{4+x}O_{54}$ and NiO in the processing steps before *in-situ* reduction to elemental Ni. Instead, $LaCrO_3$-based materials with infiltration of Ni after sintering are being explored.[94, 95]) From the XEDS maps in Figure 6.1, it is possible to conclude that La diffused into the SiO_2 substrate and formed a secondary phase.

The images in Figure 6.2 were recorded at the interface between the electrolyte and air electrode (fuel cell cathode) of a symmetric test cell. Proton-conducting $BaCe_{0.2}Zr_{0.7}Y_{0.1}O_3$ makes up the electrolyte and porous backbone in the electrode. The air electrode is covered by particles (about 100 nm in diameter) of electron-conducting $LaCoO_3$. $LaCoO_3$ is a mixed oxygen ion/electron conductor at temperatures above 600°C, but a pure electron conductor at the intended operating temperature. The electron conducting phase was synthesized by CSD infiltration to avoid cation inter-diffusion which constitutes a risk at higher processing temperatures.

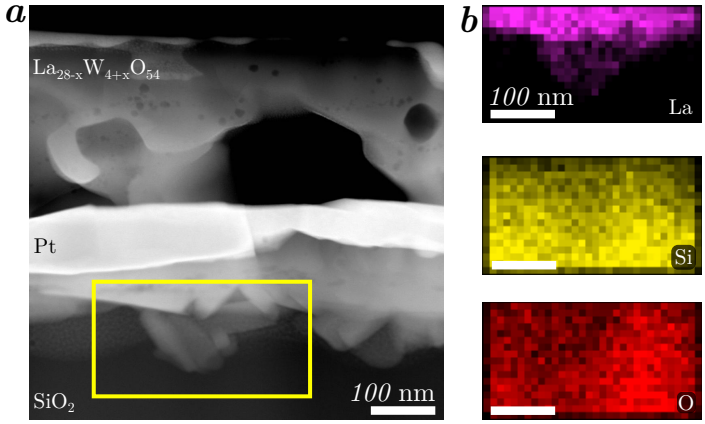

Figure 6.1: The interfaces between the SiO_2 substrate, the Pt contact and porous $La_{28-x}W_{4+x}O_{54}$ in a test cell. (a) Scanning transmission electron microscopy image in which a varying contrast is visible in the lower part of the image, in what was expected to be a single phase SiO_2. (b) XEDS element maps of the rectangular area marked in (a). La diffused into the SiO_2, probably through an opening in the Pt contact.

A simplified description of the oxygen reduction reaction in PC-SOFCs is the following: O_2 is adsorbed at the air electrode (cathode), reduced and desorbed as water vapor.[96] Table 6.1 lists the main reaction steps.

Table 6.1: Simplified elementary reaction steps for oxygen reduction at the air electrode in proton-conducting solid oxide fuel cells. TPB stands for triple phase boundary.[97, 98]

reaction steps
(1) adsorption: $O_2\ (g) \rightarrow O_2\ (ad)$ (2) dissociation: $O_2\ (ad) \rightarrow 2O\ (ad)$ (3) surface diffusion of $O\ (ad)$ to the TPB (4) bulk diffusion of H^+ from the electrolyte to the TPB (5) reduction at the TPB: $O\ (ad) + 2H^+\ (s) + 2e^- \rightarrow H_2O\ (ad)$ (6) desorption: $H_2O\ (ad) \rightarrow H_2O\ (g)$
overall reaction: $O_2\ (g) + 4H^+\ (s) + 4e^- \rightarrow 2H_2O\ (g)$

In PC-SOFC air electrodes, H_2O is formed at the triple phase boundaries (TPBs) which are present throughout the electrode as long as proton-conducting phases are included. Oxygen vacancies have been assumed to take part in the oxygen reduction reaction as catalytic centers (i.e., the vacancies are reformed after water desorption), even though they are not needed for the

overall reaction, see Table 6.1.[99] The results obtained for the test cell seen in Figure 6.2 show that oxide ion conduction (oxygen vacancies) is not necessary, as long as the material exhibits good oxygen dissociation properties.

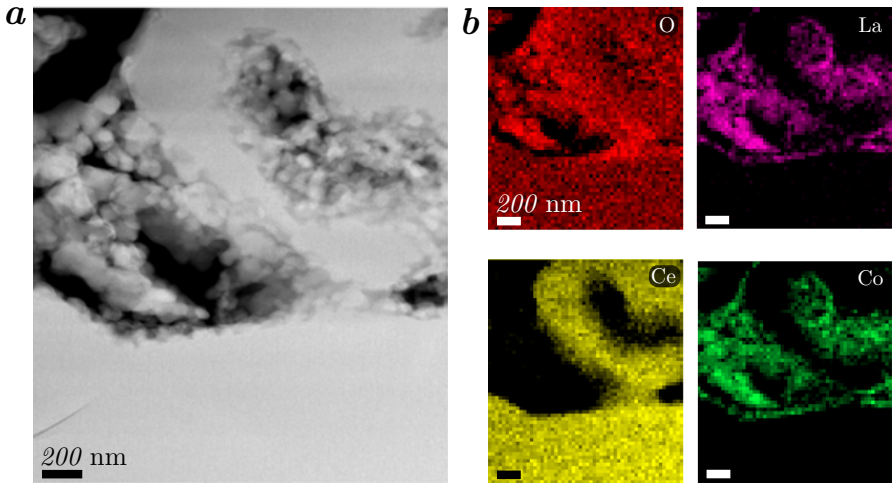

Figure 6.2: The interface between air, electrode and electrolyte in a test cell for a proton-conducting solid oxide fuel cell [VIII]. Nanosized particles of $LaCoO_3$ cover the electrolyte and porous backbone of $BaCe_{0.2}Zr_{0.7}Y_{0.1}O_3$. (a) Scanning transmission electron microscopy image and (b) XEDS element maps of the same area as in (a). [Note that the scale bar in Fig. 5 in [VIII] contains a printing error.]

Due to possible cation interdiffusion (especially Co and La into the electrolyte), which would lead to erroneous analysis of the data, it is important to thoroughly investigate whether interdiffusion has occurred. According to Figure 6.2, there was no overlap of the Ce-map with either the La- or Co-maps. This indicates that the two phases were chemically separated and that no interdiffusion occurred. Since these types of maps do not show the absolute occurrence of atom species, but rather their relative amount, full quantification tables are necessary to verify the lack of interdiffusion, and such full quantifications are performed by fitting reference spectra to the recorded spectrum. This removes the contribution from overlapping peaks to a large extent. Table 6.2 presents the results from such quantifications. The two measurements were recorded from either side of the interface. Ba and Zr were found in the electron conducting phase, but this could also be attributed to a high background signal from the proton-conducting phase. More importantly, both La and Co were below quantification the limit on the $BaCe_{0.2}Zr_{0.7}Y_{0.1}O_3$ electrolyte side of the interface.

Table 6.2: Atomic percentage of elements on either side of the interface between $BaCe_{0.2}Zr_{0.7}Y_{0.1}O_3$ electrolyte and the $LaCoO_3$ nanoparticles [VIII]. The two spectra were recorded 30 nm apart. La and Co were below the quantification limit in the proton-conducting phase. The negative amount of Y reported for the nanoparticles is an artifact of the quantification algorithm.

phase	O	La	Co	Ba	Ce	Zr	Y	total
proton conducting	49.2	0.0	0.7	26.0	5.2	16.8	2.1	100.0
electron conducting	51.5	17.5	17.8	8.4	0.9	4.7	-0.8	100.0

The STEM XEDS method has many strengths, such as compact detectors, ease of use and that all elements heavier than Be can be detected and analyzed independently. A few of its weaknesses include overlapping peaks and channeling effects in crystal structures (the latter can, however, be used for site distribution analysis [100]). Only a small fraction of the generated X-rays can be collected, which leads to noisy data, long acquisition times and beam damage.

Using SAED to observe secondary phases

Similar compounds with slightly different chemical composition often have noticeably different lattice parameters. When phase interdiffusion has occurred, the lattice parameter is expected to display a gradient towards the interface, according to Vegard's law. It is therefore often possible to observe secondary phases using diffraction. Diffraction is generally thought of as an X-ray based technique (XRD), but in some cases electron diffraction has advantages over XRD, especially when combining electron diffraction and TEM imaging. When using selected area electron diffraction (SAED), patterns from areas as small as 100–200 nm in diameter are usually recorded. Much higher spatial resolution can be achieved using nano-beam diffraction (about 10 nm) and convergent beam electron diffraction (1–2 nm).[101]

Figure 6.3 displays an overview image of a hydrogen separation membrane, sintered using spark plasma sintering. The phases present are proton-conducting $BaCe_{0.2}Zr_{0.7}Y_{0.1}O_3$ and electron-conducting $Sr_{0.95}Ti_{0.9}Nb_{0.1}O_3$. An all-ceramic composite in these types of membranes benefits from high resistance to corrosive or otherwise damaging environments.[90] Three profile plots of rotationally averaged SAED patterns are also featured in the figure, where two profiles are from single-phase areas and one is from an interface region. Since the grain size is smaller than the selection areas, the diffraction patterns are similar to powder patterns with rings rather than individual diffraction spots. Both phases have the perovskite structure but with different lattice

parameters. The two phases have different average grain sizes resulting in less dense rings of the SAED pattern from the larger grained $Sr_{0.95}Ti_{0.9}Nb_{0.1}O_3$, and fewer contributions from some crystal planes. The difference in grain size between the phases can be due to insufficient mixing of the powders before sintering or non-homogeneous sintering conditions.

The SAED for the single phase areas include the expected diffraction *peaks* from perovskite (cubic primitive symmetry) with lattice parameters in agreement with the compositions. The SAED from the interface area includes double-*peaks* in compliance with both phases, with the addition of two unidentified *peaks*. The typical *peak* shoulders that often appears in profiles from secondary phases is not seen. However, as the reciprocal spatial resolution is low, secondary phases cannot be ruled out.

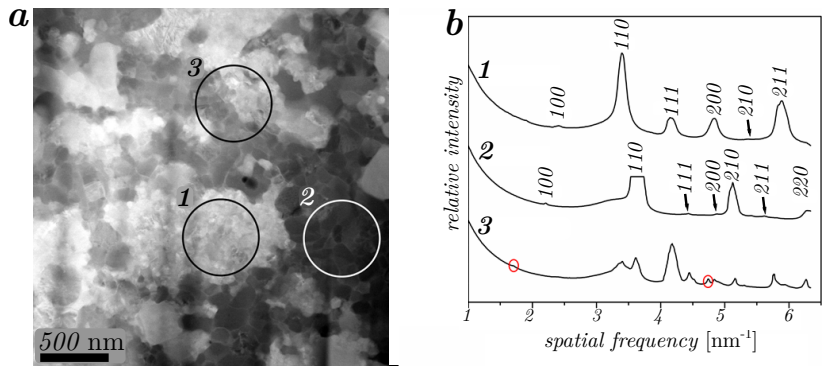

Figure 6.3: Mixed phase material with proton-conducting $BaCe_{0.2}Zr_{0.7}Y_{0.1}O_3$ (1) and electron-conducting $Sr_{0.95}Ti_{0.9}Nb_{0.1}O_3$ (2) [IX]. (a) Scanning transmission electron microscopy image with circles highlighting the three areas used for SAED. 1: Proton-conducting phase only, 2: electron-conducting phase only, and 3: an interface between the two phases. (b) The corresponding selected area electron diffraction radial intensity profiles. The 110 *peak* for the electron conducting $Sr_{0.95}Ti_{0.9}Nb_{0.1}O_3$ phase (2) has been truncated due to detector saturation. The two marked *peaks* in the interface profile (3) were not identified. All other *peaks* in profile (3) were aligned with the primary phases.

The strengths of SAED include its speed of use, high spatial resolution, and the possibility to combine it with TEM imaging. One of its weaknesses is that the best accuracy is achieved either for single crystal diffraction on a zone axis, or for powder-like samples where the grains are much smaller than the selected area. Situations that fall between such cases tend to include features from both scenarios, meaning few, high-intensity spots from grains on the zone axis while at the same time there are too many spots to properly identify individual ones.

Using HRTEM to observe secondary phases

The detection of potential secondary phases by HRTEM is mostly done by local lattice parameter measurements (also referred to as strain analysis). This is often done by measuring changes in atom positions directly in the images (peak fitting method [102]), or using the Fourier transforms of the images (described below). In Figure 6.4, a HRTEM image shows the hydrogen separation membrane mentioned earlier in the SAED-section. The interface between the proton-conducting $BaCe_{0.2}Zr_{0.7}Y_{0.1}O_3$ and the electron-conducting $Sr_{0.95}Ti_{0.9}Nb_{0.1}O_3$ is imaged edge-on. The $BaCe_{0.2}Zr_{0.7}Y_{0.1}O_3$ lattice is aligned with a $\langle 110 \rangle$ direction parallel to the beam, while the $Sr_{0.95}Ti_{0.9}Nb_{0.1}O_3$ is not oriented on a zone axis.

HRTEM images can be analyzed by Fourier filtering, which is somewhat similar to dark field (DF)TEM. In DFTEM, an aperture is used to select a diffraction spot, g, in the back focal plane (or Fourier plane) of the objective lens. After switching to image mode, only the areas of the sample associated with g are bright in the image. In Fourier filtering, a mask function that removes all information except g is applied to a Fourier transform of the image. After an inverse transform, regions of the image with lattice spacings d associated with g ($d = 1/g$) are bright and clear in the image. In other words, only the image regions including lattice spacings d have amplitude, while the rest of the image is dark with zero amplitude. It is however problematic to differentiate between similar lattice spacings and very small mask openings must be used to separate neighboring spots in the Fourier transform. The smaller the mask openings, the more blurred the image will be after inverse Fourier transform. This is due to the reciprocal relationship between the image and the Fourier transform, where convolution with a narrow (mask) function in the Fourier transform is the same as multiplication with a broad function in the image.

Instead of directly observing the amplitude in the Fourier-filtered image, geometric phase analysis (GPA)[103] can be used to map out the lattice spacings in the image. When the spot g is isolated in the Fourier transform, the corresponding lattice spacing, d, can be calculated from the (geometric) phase, P_g, of the Fourier-filtered image. Figure 6.4, where (x, y) are coordinates in the image and the y-axis is perpendicular to the $\{100\}$-planes and the x-axis is perpendicular to the $\{011\}$-planes, is used as an example.

The d_{100} spacings can be calculated using equation 6.1 and the d_{011} spacings using equation 6.2:

$$\frac{1}{d_{100}(x,y)} \propto \frac{\partial P_{100}}{\partial y}(x) \tag{6.1}$$

$$\frac{1}{d_{011}(x,y)} \propto \frac{\partial P_{011}}{\partial x}(y) \tag{6.2}$$

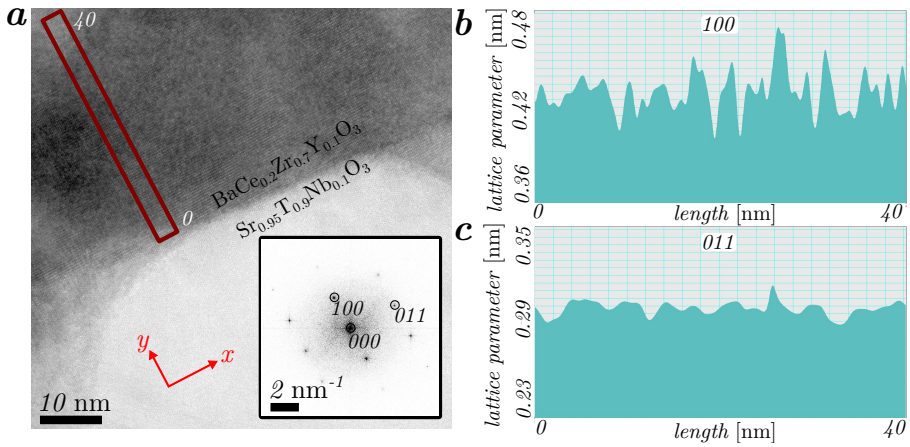

Figure 6.4: A hydrogen separation membrane, synthesized using spark plasma sintering, consisting of proton-conducting $BaCe_{0.2}Zr_{0.7}Y_{0.1}O_3$ and electron-conducting $Sr_{0.95}Ti_{0.9}Nb_{0.1}O_3$ [IX]. (a) HRTEM image of the interface between the two phases, where the $BaCe_{0.2}Zr_{0.7}Y_{0.1}O_3$ lattice is imaged in a $\langle 110 \rangle$ direction while the $Sr_{0.95}Ti_{0.9}Nb_{0.1}O_3$ has an unknown orientation. The inset is a Fourier transform of the image. (b)-(c) Geometric phase analysis (GPA) line profiles from the red area marked in (a). The analysis was done using the 100 and 011 spots labeled in the inset. No gradient in lattice parameter was observed towards the interface.

Using GPA, no shifting of lattice parameter could be measured in Figure 6.4, indicating that element interdiffusion had not taken place. The downside of this technique is that HRTEM images have small fields of view and require numerous images to investigate areas larger than about 100×100 nm^2 (using a 2048×2048 pixel camera sensor). Additionally, contrast in HRTEM images may be altered by FIB-induced damage, which increases the noise. For epitaxial phases, it can also be hard to know whether a change in lattice parameter is due to a change in composition or to strain at the interface, even though thin lamellae help stress relaxation in such cases [104].

7 Outlook

The greater our knowledge increases
the greater our ignorance unfolds.

— John F. Kennedy [105]

Over the past decade, the resolution achievable by transmission electron microscopy and scanning transmission electron microscopy (S/TEM) has been improved by hardware aberration correction. Both probe correctors and image correctors provide sub-Ångström resolution on a regular basis.[38, 106] Another advantage is that atomic resolution can be achieved at lower acceleration voltages, thus reducing knock-on damage.[107] As a consequence, the specimens must be thinner and of higher quality than ever before.

Focused ion beam (FIB) machining has long been the most versatile technique for preparing S/TEM specimen lamellae. But since the high-energy ions inflict damage, this technique has also been associated with poor chemical and crystal qualities.[56, 108–113] The most common ion used in FIB is Ga^+ from liquid metal ion sources (LMIS).[114] However, it is not the ideal choice for preparing III–V semiconductor material due to the reaction between Ga and other group 13 elements. Ga^+ bombardment can alter the III/V-ratio and sometimes form eutectic droplets. Using Ga^+-FIB under cryo-conditions, where the sample is cooled to about -135° C, has been proposed as, and to some extent shown to be, a solution to this problem.[115, 116] But the benefits of using cryo-FIB seem to decrease, or even disappear, after the material is brought back to room temperature. It is therefore recommended that the specimen be kept cool for the entire process from FIB to S/TEM, making this a cumbersome method.[117]

Another solution is to use non-Ga sources, either for the preparation of the entire lamella or for the final thinning and polishing. Gas field ion sources (GFIS) provide ionized gases such as He^+, Ne^+, and Ar^+ and plasma sources provide Xe^+ for FIB.[114, 118, 119] Noble gases have the advantage of being inert but they are, with the exception of Xe^+, light which brings the sputtering yield down and increases the processing time. To use He^+ for surface damage reduction, for example, would probably not be the best choice considering that penetration is deep and many more ions would be implanted than particles

sputtered.[120] By using a liquid metal alloy ion source (LMAIS) with a Wien mass filter (E × B filter), ions such as Au^+, Si^+, and Be^+ are made available in a interchangeable manner.[121] This offers the ability to use the best suited ion at the different processing steps, thus optimizing for both milling rate and lamella quality.[122]

Different techniques are being explored in order to keep up with the thickness demands from microscope operators. For instance, stages with swing/flip axis motion can help remove curtain effects. The flip motion changes the beam's angle of incidence, while the swing motion rotates the lamella around a fixed incident angle, thus rotating the polishing angle. The continuous shifting of the polishing angle can smooth out shadow effects that are due to topography or different material etch rates.[123] In the X^2 method, the lamella is rotated 90° between polishing of the front and back. Only the rectangle that is polished on both sides is thinned for S/TEM while the surrounding material is left as a supporting frame. This facilitates lamellae which are thinner than 10 nm and larger than 2×2 μm^2 to be stable without much bending or warping.[55, 124]

The most likely way forward, towards thinner lamellae of higher quality, is by a two-step process: first FIB chunk milling and lift-out using equipment capable of high sputtering rates and high precision (like LMIS Ga^+), followed by a final thinning and polishing using specialized equipment.

During thinning and polishing, three main issues should be considered: 1) the incident angle, 2) the acceleration voltage, and 3) the ion species. Improving the use of the incident and polishing angles would require more complex stage platforms including, for example, the swing/flip motion mentioned earlier. The acceleration voltage should be as low as possible. A reduction of surface damage after polishing with low energy Ga^+, Ar^+, and Xe^+ has been reported [120, and references therein]. However, which ionic species that works best for which sample has yet to be determined. With the exception of low-energy Ar^+ polishing, non-Ga^+ or multispecies instruments have not been in frequent use long enough. Low-energy Ar^+ polishing seems to provide satisfactory results for most samples and is the method most researchers settle for. But there might be an even better technique, known as cluster ion beam (CIB) polishing, which is today mainly used for surface smoothing and high-resolution ion sputtering depth profiling (SDP). These clusters can be large molecules, such as $B_{10}H_{14}$ or C_{60}, or gas clusters of small molecules or atoms such as N_2, SF_6 or Ar. The gas clusters are formed when pressurized gas is injected into a vacuum system through a designed nozzle and an adiabatic expansion eventually causes the atoms or molecules to coalesce. The clusters

are then weakly ionized by electron bombardment and accelerated towards a target.[125]

A $B_{10}H_{14}$ ion accelerated to 5 keV has a similar penetration depth to a single B^{3+} accelerated to 500 eV, and a 20-keV Ar_{2000}-cluster contains an average energy of only 10 eV/atom. This is the *equivalent low energy* effect experienced when accelerating large clusters. CIB polishing differs from single ion beam (SIB) polishing in that a larger amount of energy is more rapidly deposited in a smaller and more shallow volume. However, the individual atoms in the clusters are not energetic enough to cause sub-surface damage. CIB can therefore smooth surfaces by lateral distribution sputtering, a mechanism not available in SIB. Also, CIB has a higher sputtering yield, about 10-100 times greater for Ar-clusters than for single Ar^+ ions.[126–129] Reduction of both crystal damage and chemical damage has been reported for Ar-clusters when compared to single Ar^+ beams.[130, 131] During CIB bombardment, crater-like structures appear on the target surface, and consequently either smoothing or roughening can be achieved, where the final result depends on the cluster size, energy per atom and number of impacts [132]. Such craters are formed by shallow sputtering and almost no amorphous phase can be seen in cross-sectional TEM images [133].

One of the major differences between polishing by SIB and CIB is the incident angle. With the exception of chemically reactive gas clusters [134,135], CIB should have an incident angle that is nearly normal to the surface [129], while SIB should have an incident angle almost parallel to the surface [136]. Lamellae polished using CIB would thus have *face on* impact, as oppose to *edge on* impact in traditional FIB polishing. How this might affect the polishing of thin lamella for S/TEM purposes is hard to predict. Possible benefits of *face on* polishing could be the formation of completely parallel lamella surfaces and the fact that structures in different areas of the lamella would receive equal treatment. The lamella thickness might be more controllable and shadow effects could also be eliminated. Such predictions have to be investigated of course, but researchers in the field expect to find explicit benefits of CIB cleaning (Takaaki AOKI, Kyoto University, personal communication, November 16, 2015). The combination of FIB and CIB processing is currently described as one of the new *hot topics* at international CIB conferences (Takuya Miyayama, ULVAC-PHI Inc., personal communication, November 16, 2015).

Populärvetenskaplig sammanfattning

Because it's there.

— George Mallory [137]

Det är huvudsakligen materialen för tre typer av energiomvandlare, *bränsleceller, solceller och lysdioder* som berörs i avhandlingen. Bränsleceller omvandlar bränsle direkt till elektricitet. Detta sker utan mekanisk rörelse vilket öppnar upp för en högre effektivitet och en längre livslängd jämfört med dagens förbränningsmotorer. I solceller är det ljus som omvandlas direkt till elektricitet och precis som bränsleceller har solceller en relativt hög effektivitet och lång livslängd. Solen är en enorm energikälla då det ljus som når jorden bär med sig all energi vi behöver för dagens samhälle. Lysdioder är, likt glödlampor, en ljuskälla men de är både effektivare och har en längre livslängd.

Mikroskop som kan avbilda små detaljer är en viktig del av forskningen för att ta fram nya material till nästa generations energiomvandlare. Transmissionselektronmikroskopet använder elektroner, på i stort sätt samma vis, som ett klassiskt mikroskop använder ljus. Den stora fördelen med att använda elektroner istället för ljus är att extremt små detaljer kan avbildas. En nackdel är dock att de material som undersöks måste vara ytterst tunna. En stor del av avhandlingsarbetet kretsar kring hur material och komponenter bör bearbetas inför transmissionselektronmikroskopering för att bli tillräckligt tunna. Utvecklingen av dessa bearbetningsmetoder har gjort det möjligt att undersöka nanostrukturer på helt nya sätt.

Nanostrukturerna är vanligtvis kristallina pelare av halvledarmaterial. Dessa utgör en av de viktigaste komponenterna i både solceller och lysdioder, alltså den komponent där ljusenergi och elektricitet omvandlas. Varje fel i kristallen drar dock ner effektiviteten. För att kunna studera kristallfel krävs mikroskopering där det går att särskilja atomer. Transmissionselektronmikroskopet klarar detta eftersom avbildningen av ett material kan ha flera miljoner gångers förstoring utan att bli suddig. Flera typer av kristallfel behandlas i

avhandlingsarbetet och resultaten har bland annat använts för att förklara varför framställning av nanostrukturer ibland går fel. Med denna nya kunskap kan vissa problem numera undvikas.

Avhandlingen behandlar även keramiska kompositer, som är vanliga i bränsleceller. Dessa kompositer består av olika keramiska material i en kombination där de olika materialegenskaperna kompletterar varandra. Ibland uppstår oväntade reaktioner som leder till nya och oönskade föreningar. Detta sker då atomer från de olika materialen vandrar in i varandra. Med transmissionselektronmikroskopet kan varje grundämne lokaliseras och genom att studera kompositernas kontaktytor går det att undersöka de nybildade föreningarna. Denna typ av grundämnesanalys ingår i avhandlingsarbetet och har resulterat i en djupare förståelse för de kemiska förloppen i en bränslecellselektrod. Detta har i sin tur medfört att fler material kan användas i bränsleceller. Med fler val blir det enklare att skräddarsy de keramiska kompositerna för att optimera dess förmåga.

Metodbeskrivning på svenska

Att vetenskaperna på detta sätt går över i varandra är typiskt för vår tid och visar vikten av samarbete över de gamla gränserna.

— Gunnar Hägg [138]

En stor del av forskningen som presenterats i denna avhandling har framkommit genom transmissionselektronmikroskopi (TEM), en teknik som Ernst Ruska började utveckla under 1930-talet. Han belönades senare med Nobelpriset i fysik för sitt arbete med elektronoptik och för konstruktionen av det första elektronmikroskopet. Tekniken använder accelererade elektroner vars hastighet ligger nära ljusets när de styrs rakt igenom objektet som studeras. Med hjälp av magnetiska linser fokuseras elektronerna som då avbildar objektet i hög förstoring. Alla objekt, så kallade prov, som ska studeras med TEM måste följaktligen vara mycket tunna för att elektronerna ska kunna passera igenom dem. En framgångsrik metod för förtunnande provpreparering görs med hjälp av en fokuserad stråle av joner (FIB, efter engelskans focused ion beam), och det är de unika resultaten som kan åstadkommas med FIB och TEM som utgör författarens bidrag i de presenterade forskningsrapporterna. Men för att kunna ta till sig denna allra senaste forskning kan det underlätta med en sammanfattande historik över händelserna som ledde hit. Vi tar det från början.

De första stegen mot mikroskopi som vetenskap togs av Galileo Galilei (född 1564) och Hans Lippershey (född ca 1570) då de modifierade sina stjärnkikare för att studera närliggande föremål. Men det avgörande framsteget togs av Zacharias Janssen (född 1585), som var glasögontillverkare, då han började använde dubbla konvexa linser i sina mikroskop. Detta har blivit den klassiska linsuppsättningen som återges i alla moderna läroböcker i optik och mikroskopi. Många ser nog Robert Hooke (född 1635) som en av de främsta pionjärerna. År 1665 publicerade han boken *Micrographia* som innehåller skisser av hans observationer med mikroskop. En skiss av själva mikroskopet kan ses i Figur 1a. Med *Micrographia* spreds nya upptäckter samtidigt som en ny generation vetenskapsmän intresserade sig för mikroskopet som vetenskapligt verktyg. Hooke är kanske mest känd för att ha myntat begreppet biologiska celler, vilket han använde för att beskriva strukturerna han såg i tunt skivad

kork. Antonie van Leeuwenhoek (född 1632), som ibland kallas mikrobiologins fader, är en annan pionjär. Han byggde flertalet instrument, bland annat ett sådant som visas i Figur 1b. Detta instrument, som består av en kopparplatta med en lins i en öppning mitt i plattan, hölls upp till ögat och riktades mot solen. På sidan av plattan som vette mot solen monterades ett prov som orienterades rätt i fokus med skruvar. Leeuwenhoek blev med sina instrument först i världen med att se bakterier (som han kallade animalcules) och mänskliga celler.

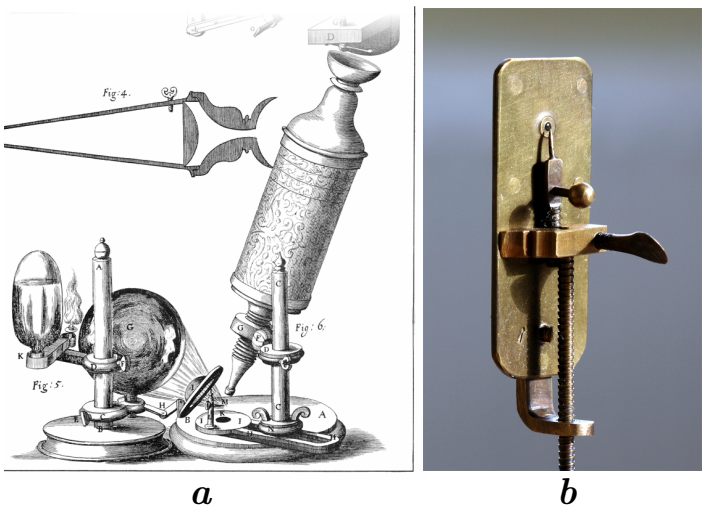

Figur 1: : (a) Robert Hookes egna skiss av sitt mikroskop, från boken *Micrographia* [138]. Instrumentet var ca 30 cm högt. (b) Replika av Antonie van Leeuwnhoeks lupp, som är ca 5 cm hög. Foto Jeroen Rouwkema, licens Creative Commons BY-SA.

Det har även skett framsteg inom mikroskopins utveckling under modern tid. Exempelvis har forskningsfältet belönats med ett flertal Nobelpris. 1925-års Nobelpris i kemi tilldelades Richard Zsigmondy (född 1865) för hans bidrag i utvecklingen av ultramikroskopet. En teknik som använder ljusets spridning, istället för reflektion, för att observera mycket små partiklar. Metoden användes bland annat för att studera Brownsk rörelse i vätska och gas. Frits Zernike (född 1888) tilldelades 1953-års Nobelpris i fysik för att ha uppfunnit faskontrastmikroskopet; en teknik som utnyttjar ett fasskifte i ljuset för att åstadkomma kontrast i bilden. Ljus som passerar genom ett genomskinligt prov, såsom biologiska celler, ger vanligtvis inte upphov till någon bild. För att studera exempelvis organeller förlitade man sig på infärgning med kontrastmedel. Sådan infärgning behövs alltså inte vid faskontrastmikroskopi.

Kontrasten uppkommer eftersom ljus rör sig med olika hastighet i olika material och två ljusstrålar kan hamna i otakt om de färdats genom olika material. Delar av provet där ljuset är i otakt blir mörka i bilden och de delar där ljuset är i fas blir ljusa. Såsom nämndes inledningsvis fick Ernst Ruska (född 1906) Nobelpriset i fysik för sitt arbete med elektronoptik och elektronmikroskop. Priset gavs år 1986, men Ruska hade redan år 1931 börjat bygga ett TEM tillsammans med Max Knoll (född 1897). En tidig skiss av det första elektronmikroskopet kan ses i Figur 2a och ett foto av det TEM som författaren använt under sin tid som doktorand kan ses i Figur 2b. TEM liknar faktiskt ett klassiskt ljusmikroskop på många sätt men belyser provet med en elektronstråle istället för en ljusstråle. Heinrich Rohrer (född 1933) och Gerd Binnig (född 1947) delade Nobelpriset i fysik 1986 med Ruska. De uppmärksammandes för sveptunnelmikroskopet. Denna teknik var vid tiden helt olik alla andra mikroskopitekniker i och med att en mycket spetsig nål leder en elektrisk ström till provets yta. Genom att mäta strömmens styrka när nålen sakta sveper över ytan kan de enskilda atomerna avbildas. År 2014 delade Eric Betzig, Stefan W. Hell och William E. Moerner Nobelpriset i kemi för sina bidrag inom utveckling av superupplöst fluorescensmikroskopi, en uppsättning tekniker som kringgår den klassiska upplösningsgränsen. Denna gräns, som härleds ur fysikens lagar, formulerades av Ernst Abbe ca år 1878 och troddes länge sätta stopp för mikroskoputvecklingen. Men i och med utvecklingen av superupplöst fluorescensmikroskopi hade pristagarna hittat sätt att kringgå Abbes upplösningsgräns.

I forskningen som presenteras här är det framförallt transmissionselektronmikroskopi (TEM) som använts. Men då TEM ställer höga krav på proven har provpreparering med FIB varit lika viktigt. FIB-processen liknar sandblästring men istället för sand används joner för att blästra bort oönskat material. Ett foto av det FIB-instrumentet som författaren använt kan ses i Figur 3.

Utvecklingen av FIB började under 1970-talet [139–141]. De första instrumenten byggdes faktiskt för jonstråleanalys och som mikroskop, utan någon direkt tanke på provpreparering.[142] Att undersöka ett material med FIB kan i många fall komplettera den mer standardiserade tekniken svepelektronmikroskopi (SEM).[143] Men då proven tar skada av jonstrålen i FIB har det aldrig blivit en särskilt populär mikroskopimetod. Bland de första att använda FIB-instrumentets unika förmåga att blästra (eller etsa) bort material med mycket hög precision var J. R. A. Cleaver med kollegor [144]. De etsade först en liten fördjupning i ett prov, ändrade sedan provets vinkel mot strålen och tog bilder av sidoväggen. Bilderna visade därmed ett tvärsnitt av vad som fanns under ytan på provet. År 1989 blev E. C. G. Kirk med kollegor först med att använda FIB för att förtunna ett prov och sedan studera det i TEM [145]. Den tunna delen av provet kallades för lamell. Denna metod krävde

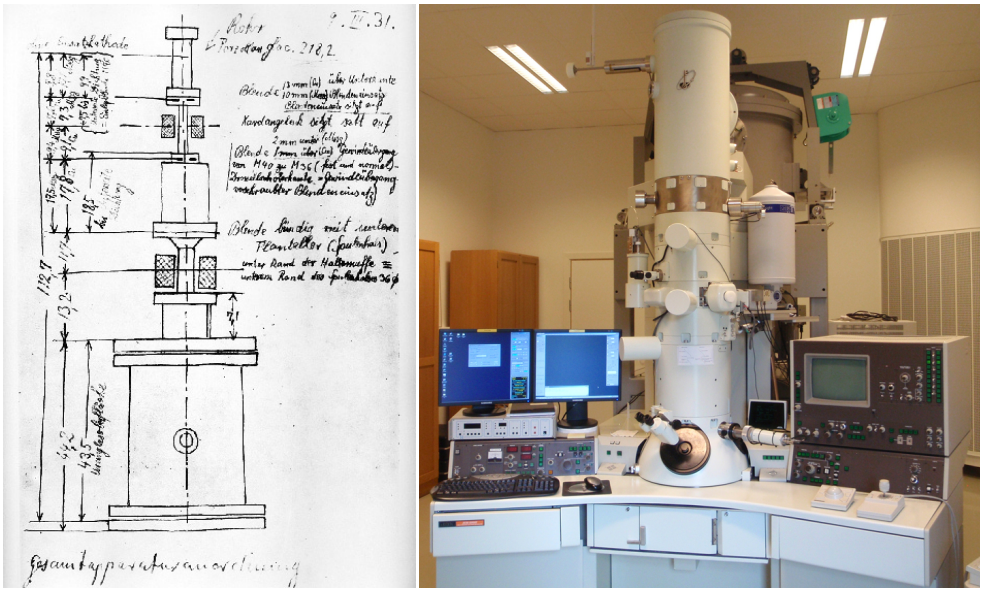

a *b*

Figur 2: (a) Ernst Ruskas egen skiss av ett tänkt transmissionselektronmikroskop, daterad den 9 mars år 1931. © The Nobel Foundation 1986. (b) Ett transmissionselektronmikroskop av modell 3000F, tillverkat av JEOL (ursprungligen Japan Electron Optics Laboratory). Mikroskopet finns vid National Center for High Resolution Electron Microscopy (nCHREM) i Lund. Instrumentet är ca 2.5 m högt.

dock mycket förberedande arbete med ett fint slippapper. I början av 1990-talet revolutionerade M. H. F. Overwijk med kollegor provpreparering genom att introducera den så kallade lamella lift-out-tekniken [146]. Tekniken går ut på att frilägga lamellen helt från omgivande material och sedan montera den på en hållare anpassad till TEM. Nu kunde man enkelt och smidigt plocka ut en lamell var som helst från vilket prov som helst. Denna teknik vidareutvecklades av L. A. Giannuzzi med kollegor några år senare [147]. Nästa stora framsteg kom 1999 när T. Ohnishi med kollegor utvecklade *in-situ* lamella lift-out (INLO)-tekniken [58], vilken gjorde det möjligt att utföra flera moment i snabb följd, utan att behöva flytta provet mellan olika instrument.

På senare tid har utvecklingen inom FIB-preparering gått mot att minska de skador som uppstår på lamellerna [47, 48]. Minskade skador har i sin tur gjort det möjligt att preparera tunnare lameller vilket ger bättre bilder i TEM. Men nya problem har uppstått eftersom en riktigt tunn lamell inte alltid kan hålla uppe sin egen vikt. En ny design med självbärande lameller, så kallade ramlameller, har börjat dyka upp i litteraturen. Bland annat har L. Lechner,

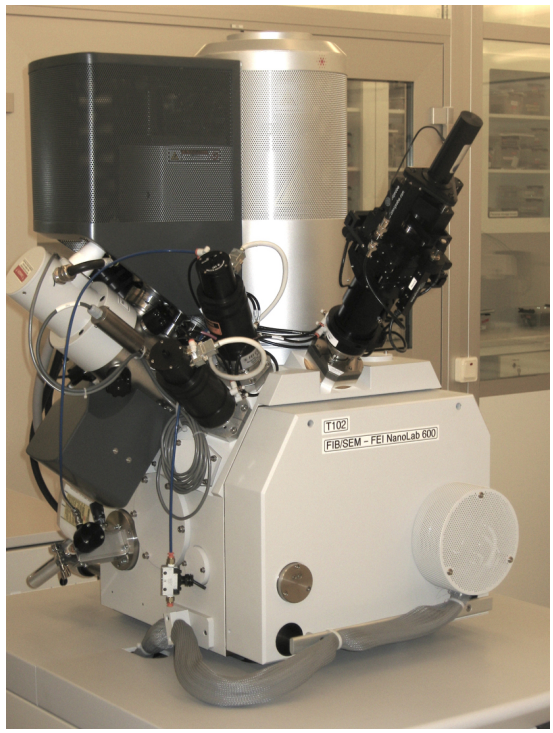

Figur 3: Ett kombinerat FIB/svepelektronmikroskop av modell Nova 600 NanoLab, tillverkat av FEI. Mikroskopet finns vid Lund Nano Lab i Lund. Instrumentet är ca 1 m högt.

N. D. Bassim, och F. Rivera med kollegor gjort bidrag.[55–57] Författarens eget bidrag har publicerats i artikeln *FIB Plan and Side View Cross-sectional TEM Sample Preparation of Nanostructures* (artikel **I** i avhandlingen).

Under detta avhandlingsarbete har olika material preparerats med FIB för vidare studier med TEM. Materialen har gemensamt att de är tillämpbara i energiomvandlare. Exempel på energiomvandlare är bränsleceller, som omvandlar kemisk energi till elektricitet, och lysdioder som omvandlar elektrisk energi till ljus. Ett typiskt keramiskt material som används i bränsleceller är bariumzirkonat ($BaZrO_3$), medan ett typiskt halvledarmaterial som används i lysdioder är galliumnitrid (GaN). Exempel på två sådana prover kan ses i Figur 4. Dessa material är mycket olika och kräver också olika typ av provpreparering.

En utmaning har varit de ömtåliga nanostrukturerna som används i lysdioder och andra komponenter av halvledarmaterial. Dessa nanostrukturer (ofta kallade nanowires på engelska) består av ytterst små kristallina pela-

re. Ibland så små som 10 nanometer i diameter och några mikrometer långa. Nanostrukturerna i Figur 4a är då relativt sett ganska stora.

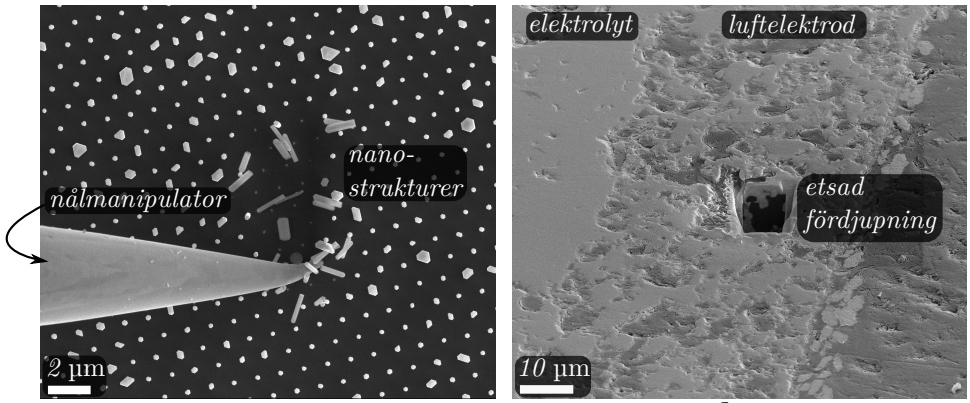

Figur 4: (a) Svepelektronmikroskopbild på nanostrukturer av galliumnitrid (GaN) stående på substratet som också består av galliumnitrid. En mycket spetsig nålmanipulator av volfram har skrapat av ett flertal nanostrukturer. (b) Svepelektronmikroskopbild föreställande den del av bränslecellen där elektrolyten möter luftelektroden. En fördjupning har etsas i elektroden med hjälp av FIB så att det går att se vad som döljer sig under ytan. Luftelektroden består av små partiklar av lantankoboltat ($LaCoO_3$) i en porös struktur av bariumzirkonat ($BaZrO_3$) med tillsatser av ceriumoxid (CeO_2) och yttriumoxid (Y_2O_3), ett material som kemiskt skrivs ut som $BaCe_{0.2}Zr_{0.7}Y_{0.1}O_3$.

Ofta är nanostrukturer tillräckligt tunna för TEM-analys i deras naturliga tillstånd och många mikroskopister nöjer sig med att undersöka dem utan någon provpreparering. Då går man dock miste om möjligheten att studera nanostrukturernas tvärsnitt och gränsytan mot substratet som de växt fram på. Att preparera nanostrukturerna kan således ge mer information, men kräver också mer arbete. För att bereda vinkelräta tvärsnitt av nanostrukturerna behöver de först packas in i ett material så att tvärsnitten hålls på plats. Detta inbäddningsmaterial får inte skada eller förändra de ömtåliga nanostrukturerna, men det måste också kunna stå emot den kraftiga elektronstrålen i mikroskopet. Spurrs epoxy, en plast som utvecklades av Arthur R. Spurr [54] i slutet av 1960-talet för att skydda biologiska celler, har visat sig vara ett lämpligt material. I Figur 5 visas några av stegen under preparering av nanostrukturer till vinkelräta tvärsnitt. Hela substratet med nanostrukturerna gjuts in i Spurrs epoxy och efter att plasten härdat poleras en sidovägg med fint slippapper tills substratet syns. För att skydda nanostrukturerna mot jonstrålen läggs ett lager metall ovanpå lamellämnet (området som kom-

mer att bli den tunna lamellen). Två fördjupningar etsas, ett i epoxyn ovanför nanostrukturerna (vilka är orienterade horisontellt) och ett i substratet under nanostrukturerna. Lamellämnet etsas sedan helt fritt från omgivande material och lyfts ur med hjälp av nålmanipulatorn (Figur 5b). Lamellämnet flyttas till en annan del av FIB-instrumentet och monteras på en hållare som är anpassad för TEM (Figur 5c). Polering sker på båda sidor tills en tunn lamell återstår (Figur 5d-e). I exemplet i figuren så har poleringen skett i en låg vinkel mot substratytan som nanostrukturerna växt på. Detta innebär att tvärsnitten på vänster sida av lamellen kommer från de nedre segmenten av nanostrukturerna medan tvärsnitten på höger sida kommer från de övre segmenten (Figur 5f).

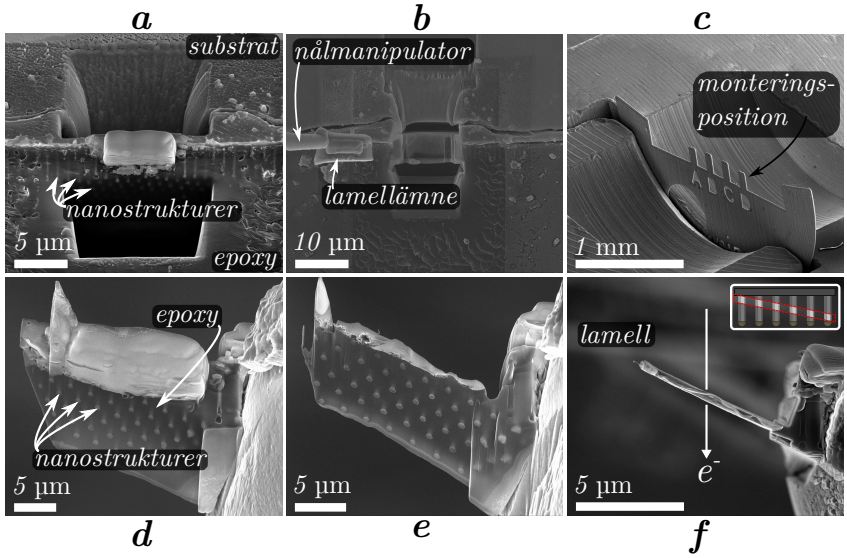

Figur 5: Svepelektronmikroskopbilder som visar hur vinkelräta tvärsnitt prepareras av nanostrukturer med hjälp av FIB INLO. (a) En skyddande metall placeras ovanpå den blivande lamellen (lamellämnet) och två fördjupningar etsas på var sida om lamellämnet. Bilden är tagen snett ovanifrån. (b) Lamellämnet etsas fritt och flyttas sedan med hjälp en nålmanipulator. Bilden är tagen rakt ovanifrån. (c) Lamellämnet monteras på en TEM-anpassad hållare. (d)-(e) Efter polering återstår en tunn lamell. Bilderna är tagna snett ovanifrån. (f) Polering kan göras så att tvärsnitten placeras olika på olika nanostrukturer. Bilden är tagen rakt ovanifrån och en skiss av nanostrukturerna är infogad i överkanten.

Det går att göra flera typer av TEM-undersökningar på dessa tvärsnitt. Några nämnvärda metoder är energiupplöst röntgenspektroskopi (XEDS), elektrondiffraktion (SAED) och högupplöst transmissionselektronmikroskopi (HRTEM). Resultat från dessa tekniker kan ses i Figur 6. Med XEDS är det

bland annat möjligt att skapa en slags karta över de grundämnen som finns i provet. Med SAED observerar man hur elektroner sprids när de går igenom provet. Mönstren som uppstår visar bland annat hur nära varandra atomerna sitter. Med HRTEM-tekniken är det möjligt att se atomerna direkt.

Nanostrukturerna, som syns i Figur 6 (a)-(b), har en stavformad sexkantig kärna av indiumfosfid (grönt område) omgiven av ett flertal skal. Första skalet består av indiumaluminiumfosfid, $Al_{0.25}In_{0.75}P$ och $Al_{0.50}In_{0.50}P$, (rött område) och omsluts av ett skal av aluminiumoxid (blått område). Tanken var att indiumaluminiumfosfiden skulle utgöra ett isolerande skal i en solcellkomponent men undersökningen visade att skalet oxiderar. Delar av ett oxideringsskyddande lager av indiumfosfid kan ses i Figur 6a, men detta skal lyckades inte täcka hörnen ordentligt.

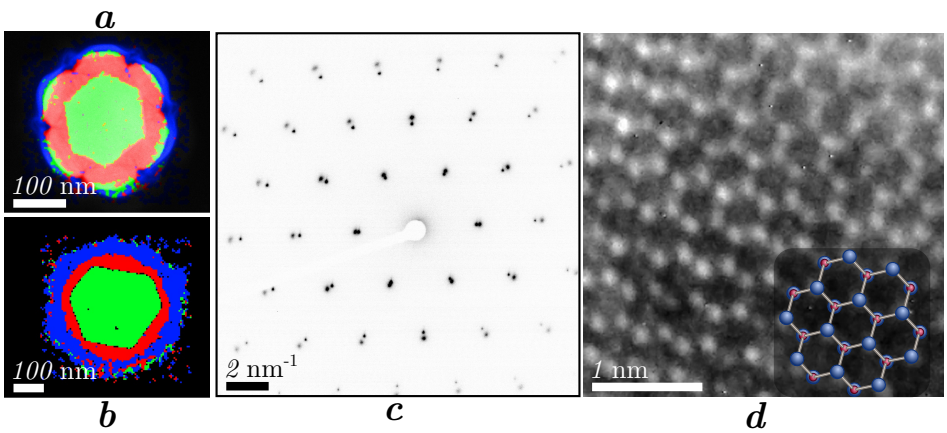

Figur 6: Olika transmissionselektronmikroskopitekniker applicerade på vinkelräta tvärsnitt av nanostrukturer. (a)-(b) Kombinerad (svep)transmissionselektronmikroskopi och energiupplöst röntgenspektroskopi, som ger kartor över olika grundämnen. Den gröna färgen visar var halvledarmaterialet indiumfosfid (InP) finns, den röda färgen var halvledarmaterialet indiumaluminiumfosfid ($In_{1-x}Al_xP$) finns och den blå färgen var aluminiumoxid finns. (c) Elektrondiffraktion från provet i panel (b). Mönstret visar på sextalig symmetri av två material med olika atomavstånd, vilket beror på att atomerna i InP sitter något glesare än atomerna i $Al_{0.50}In_{0.50}P$. (d) En högupplöst transmissionselektronmikroskopibild som visar en liten del av nanostrukturen i panel (a), där atomerna avbildats som ljusa fläckar. En atommodell är infogad nere till höger på bilden.

Eftersom lameller är så tunna finns det risk att de böjs eller deformeras. I sådana fall är det lämpligt att använda en design där den tunna lamellen stabiliseras av ett ramverk. En sådan ramlamell kan ses i Figur 7, där tvärsnitt av nanostrukturerna för granskning från sidan har preparerats. De snittades

på längden så att gränsytan mellan nanostrukturerna och substratet kunde undersökas. Processen liknar den tidigare nämnda preparationsmetoden för vinkelräta tvärsnitt, med skillnaden att nanostrukturerna orienterades stående istället för liggande. I Figur 8 visas resultat från en TEM-undersökning av tvärsnitt med sidovy. Nanostrukturerna har en kärna av galliumarsenid (GaAs) med ett skal av galliumindiumfosfid ($Ga_{1-x}In_xP$).

En lamell för TEM-analys har en uppenbar begränsning i det att endast en mycket tunn skiva undersöks. Nästan ingen tredimensionell information om provet kan fås fram genom TEM. En lösning på denna begränsning är att kombinera TEM med en annan karakteriseringsmetod kallad FIB-tomografi.[148, 149] FIB-tomografi kan dock inte ersätta TEM då den inte ger lika detaljrik information. Proceduren går ut på att etsa en fördjupning i provet och ta en bild av en sidovägg. Som nämnts tidigare får man då kännedom om hur ett tvärsnitt under ytan ser ut. Genom att iterativt förstora fördjupningen och ta nya bilder kan man bilda sig en uppfattning av hur det ser ut i många angränsande tvärsnitt. Om detta görs systematiskt kan bilderna läggas ihop till en slags 3D-modell.

Figur 9 visar ett exempel på en bränslecell bestående av nickel och ett keramiskt material kallat YSZ (efter engelskans yttria-stabilized zirconia). YSZ består av zirkoniumoxid (ZrO_2) med en viss mängd yttriumoxid (Y_2O_3) och är besläktat med kubisk zirkonia (eller cubic zirconia) som används i smycken. En hästskoformad fördjupning etsades i provet och FIB-tomografin utfördes sedan på det block av material som var kvar i mitten av fördjupningen. Bilder togs av blockets sida medan jonstrålen sakta polerade sidoväggen. Efter att FIB-tomografin var klar kunde den sista avbildade sidoväggen prepareras till en TEM-lamell. På så sätt kan man kombinera det bästa av båda teknikerna: information i tre dimensioner från FIB-tomografi och oerhört detaljrik information i två dimensioner från TEM. I Figur 10 visas några resultat från FIB-tomografi och TEM analys. 3D-modellen i 10a kommer från ett annat prov (då originalbilderna innehöll företagskänslig information) men är typisk för FIB-tomografi. Strukturen visar de håligheter som släpper fram vätgasen eller luften genom elektroderna. I TEM kan nickelmetall och YSZ undersökas i detalj.

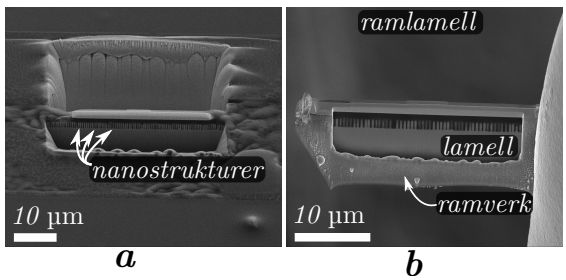

Figur 7: Svepelektronmikroskopbilder över hur tvärsnitt av nanostrukturer för granskning i sidovy prepareras med hjälp av FIB INLO [I]. (a) En skyddande metall placerades ovanpå lamellämnet och två fördjupningar etsades på var sida. Bilden är tagen snett ovanifrån. Lamellämnet frigjordes sedan och monterades på en TEM-hållare. (b) Lamellämnet polerades så att ett ramverk stabiliserade den tunna lamellen.

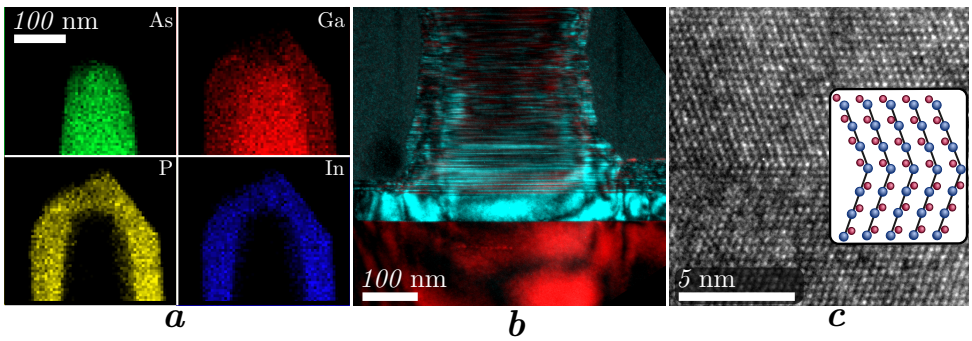

Figur 8: Olika transmissionselektronmikroskopitekniker applicerade på tvärsnitt av nanostrukturer för granskning i sidovy [I]. (a) Kartläggning med hjälp av energiupplöst röntgenspektroskopi av olika grundämnen som finns i toppen av en nanostruktur. (b) Gränsytan mellan nanostrukturen och substratet avbildad i mörkfältsläge där det går att skilja mellan olika kristaller (blått och rött i bilden). (c) En liten del av samma gränsyta avbildad med högupplöst transmissionselektronmikroskopi. De två kristallerna möts mitt i bilden och en modell av kristallerna är infogad till höger i bilden.

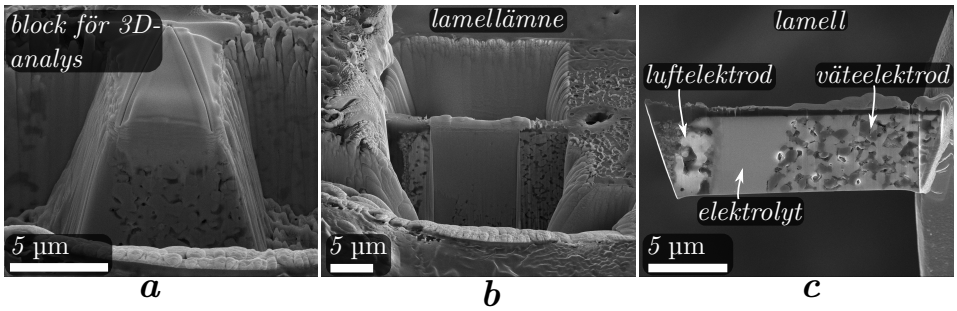

Figur 9: Svepelektronmikroskopbilder av provberedning för kombinerad FIB- tomografi och TEM-analys. Undersökningen gjordes där väteelektroden möter elektrolyten i en keramisk bränslecell. (a) En hästskoformad fördjupning etsades ut med hjälp av FIB och kvar fanns sedan ett block av material. Den inristade V-formationen på toppen av blocket hjälper datorn att pussla ihop alla bilder till en 3D-modell. (b) Efter att FIB-tomografin är klar, etsas en ny fördjupning så att ett lamellämne bildas. Den TEM-undersökning som gjordes av lamellen kommer således att passa ihop med 3D-modellen som togs fram genom FIB-tomografi. (c) Lamellämnet görs iordning för TEM genom INLO. Prov från Saan Energi AB.

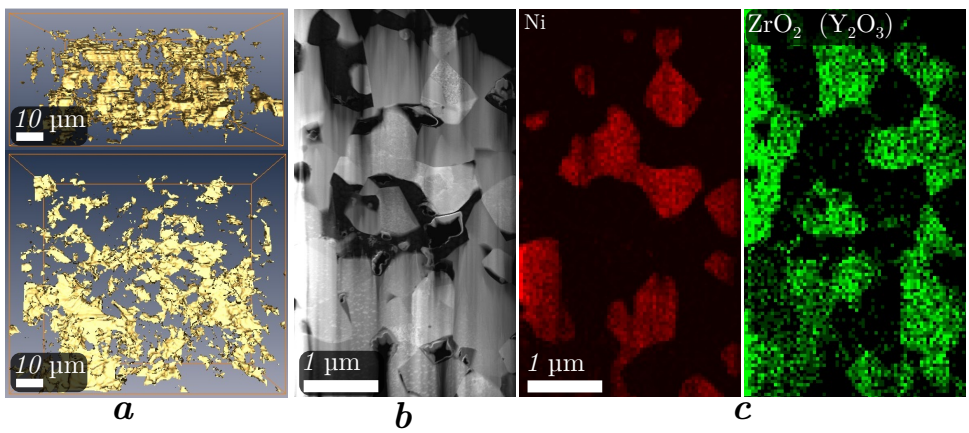

Figur 10: (a) Tredimensionell rekonstruktion sedd från två håll. Bilderna visar hur porer är sammankopplade för att släppa fram gaser. (b) (Svep)transmissionselektronmikroskopbild av en väte-elektrod. (c) Energiupplöst röntgenspektroskopi analys som visar var nickel (Ni) och YSZ (ZrO2 med en liten mängd Y2O3) finns i (b). Prov från Saan Energi AB.

References

[1] (Film), "Apollo 13", R. Howard (Dir.) and W. von Huene (Perf.), Universal Pictures, Los Angeles, California, USA and Imagine Entertainment, Beverly Hills, California, USA (1995)

[2] O. L. Krivanek et al., "Atom-by-atom structural and chemical analysis by annular dark-field electron microscopy", *Nature* **464** (2010) 571–574

[3] M. Bar-Sadan, J. Barthel, H. Shtrikman, and L. Houben, "Direct imaging of single Au atoms within GaAs nanowires", *Nano Letters* **12** (2012) 2352–2356

[4] D. B. Williams and C. B. Carter, *Transmission Electron Microscopy: A Textbook for Materials Science*, Springer, City of New York, New York, USA, 2nd edition (2009)

[5] L. Reimer and H. Kohl, *Transmission Electron Microscopy Physics of Image Formation*, Springer, City of New York, New York, USA, 5th edition (2008)

[6] S. M. Sze, *Semiconductor Devices: Physics and Technology*, John Wiley & Sons, Hoboken, New Jersey, USA, 2nd edition (2002)

[7] J. Larminie and A. Dicks, *Fuel Cell Systems Explained*, John Wiley & Sons, Hoboken, New Jersey, USA, 2nd edition (2003)

[8] K. Tomioka, M. Yoshimura, and T. Fukui, "A III-V nanowire channel on silicon for high-performance vertical transistors", *Nature* **488** (2012) 189–192

[9] T. S. Zheleva, O. H. Nam, W. M. Ashmawi, J. D. Griffin, and R. F. Davis, "Lateral epitaxy and dislocation density reduction in selectively grown GaN structures", *Journal of Crystal Growth* **222** (2001) 706–718

[10] J. Wallentin et al., "InP nanowire array solar cells achieving 13.8% efficiency by exceeding the ray optics limit", *Science* **339** (2013) 1057–1060

[11] P. P. V. Kamat, "Quantum dot solar cells. The next big thing in photovoltaics", *The Journal of Physical Chemistry Letters* **4** (2013) 908–918

[12] M. Biswas, H. Xie, and P.-C. Su, "Low temperature synthesis of sub-micrometer yttria-doped barium zirconate thin films by modified chemical solution deposition technique", *ECS Transactions* **68** (2015) 481–488

[13] H. Matsumoto, Y. Kawasaki, N. Ito, M. Enoki, and T. Ishihara, "Relation between electrical conductivity and chemical stability of $BaCeO_3$-based proton conductors with different trivalent dopants", *Electrochemical and Solid-State Letters* **10** (2007) B77–B80

[14] K. Katahira, Y. Kohchi, T. Shimura, and H. Iwahara, "Protonic conduction in Zr-substituted $BaCeO_3$", *Solid State Ionics* **138** (2000) 91–98

[15] S. M. Haile, "Fuel cell materials and components", *Acta Materialia* **51** (2003) 5981–6000

[16] L. Malavasi, C. A. J. Fisher, and M. S. Islam, "Oxide-ion and proton conducting electrolyte materials for clean energy applications: structural and mechanistic features", *Chemical Society Reviews* **39** (2010) 4370–4387

[17] E. Fabbri, D. Pergolesi, S. Licoccia, and E. Traversa, "Does the increase in Y-dopant concentration improve the proton conductivity of $BaZr_{1-x}Y_xO_{3-\delta}$ fuel cell electrolytes?", *Solid State Ionics* **181** (2010) 1043–1051

[18] K. D. Kreuer, "Proton-conducting oxides", *Annual Review of Materials Research* **33** (2003) 333–359

[19] L. Bi, S. Boulfrad, and E. Traversa, "Steam electrolysis by solid oxide electrolysis cells (SOECs) with proton-conducting oxides", *Chemical Society Reviews* **43** (2014) 8255–8270

[20] L. B. Kong et al., *Transparent Ceramics*, Springer, Switzerland (2015)

[21] T. Norby, R. Haugsrud, A. F. S. (Editor), and M. V. M. (Editor), *Nonporous Inorganic Membranes: For Chemical Processing*, John Wiley & Sons, Hoboken, New Jersey, USA (2006)

[22] J. S. Fish, S. Ricote, R. O'Hayre, and N. Bonanos, "Electrical properties and flux performance of composite ceramic hydrogen separation membranes", *Journal of Materials Chemistry A* **3** (2015) 5392–5401

[23] B. Hammack, S. Kranz, and B. Carpenter, *Albert Michelson's Harmonic Analyzer: A Visual Tour of a Nineteenth Century Machine that Performs Fourier Analysis*, Articulate Noise Books, Chicago, Illinois, USA (2014)

[24] G. L. Tuin et al., "Valence band splitting in wurtzite InP nanowires observed by photoluminescence and photoluminescence excitation spectroscopy", *Nano Research* **4** (2011) 159–163

[25] J. Arbiol et al., "Triple-twin domains in Mg doped GaN wurtzite nanowires: structural and electronic properties of this zinc-blende-like stacking", *Nanotechnology* **20** (2009) 145704

[26] C. Hammond, *The Basics of Crystallography and Diffraction*, Oxford University Press, City of New York, New York, USA, 3rd edition (2009)

[27] G. B. Stringfellow, *Organometallic Vapor-Phase Epitaxy, Theory and Practice*, Academic Press, San Jose, California, USA (1999)

[28] N. P. Dasgupta et al., "25th anniversary article: semiconductor nanowires–synthesis, characterization, and applications", *Advanced Materials* **26** (2014) 2137–84

[29] R. W. Schwartz, T. Schneller, and R. Waser, "Chemical solution deposition of electronic oxide films", *Comptes Rendus Chimie* **7** (2004) 433–461

[30] T. Schneller, R. Waser, M. Kosec, and D. Payne, *Chemical Solution Deposition of Functional Oxide Thin Films*, Springer, Vienna, Austria (2013)

[31] C. Duan et al., "Readily processed protonic ceramic fuel cells with high performance at low temperatures", *Science* **349** (2015) 1321–1326

[32] M. Nygren and Z. Shen, "On the preparation of bio-, nano- and structural ceramics and composites by spark plasma sintering", *Solid State Sciences* **5** (2003) 125–131

[33] Z. A. Munir, U. Anselmi-Tamburini, and M. Ohyanagi, "The effect of electric field and pressure on the synthesis and consolidation of materials: a review of the spark plasma sintering method", *Journal of Materials Science* **41** (2006) 763–777

[34] (Film), "The Secret Life of Chaos", N. Stacey (Dir.), J. Al–Khalili (Perf.) and I. Stewart (Perf.), British Broadcasting Corporation, London, UK (2010)

[35] B. Fultz and J. Howe, *Transmission Electron Microscopy and Diffractometry of Materials*, Springer, Berlin, Germany, 3rd edition (2008)

[36] F. Lenrick, *Wires, Voids and Particles Focused ion beam sample preperation of nanostructures*, (Licentiate thesis), Lund University, Lund, Sweden (2014)

[37] X. Zou, *Electron Crystallography of Inorganic Structures – Theory and Practice*, (Doctoral Thesis), Stockholm University, Stockholm, Sweden (1995)

[38] O. L. Krivanek, T. C. Lovejoy, and N. Dellby, "Aberration-corrected STEM for atomic-resolution imaging and analysis", *Journal of Microscopy* **259** (2015) 165–172

[39] D. Shechtman, "Al - 25% Mn, April 8 1982", *Shechtman's NBS TEM logbook records,* National Bureau of Standards, Gaithersburg, Maryland, USA (1982)

[40] C. Zheng et al., "Polarity-driven 3-fold symmetry of GaAs/AlGaAs core multishell nanowires", *Nano Letters* **13** (2013) 3742–3748

[41] D. K. Schreiber et al., "A method for directly correlating site-specific cross-sectional and plan-view transmission electron microscopy of individual nanostructures", *Microscopy and Microanalysis* **18** (2012) 1410–1418

[42] L. Mohaddes-Ardabili et al., "Self-assembled single-crystal ferromagnetic iron nanowires formed by decomposition", *Nature Materials* **3** (2004) 533–538

[43] Q. Li and G. T. Wang, "Strain influenced indium composition distribution in GaN/InGaN core-shell nanowires", *Applied Physics Letters* **97** (2010) 181107

[44] M. Fickenscher et al., "Optical, structural, and numerical investigations of GaAs/AlGaAs core-multishell nanowire quantum well tubes", *Nano Letters* **13** (2013) 1016–1022

[45] E. Luna et al., "Investigation of III–V nanowires by plan-view transmission electron microscopy: InN case study", *Microscopy and Microanalysis* **20** (2014) 1471–1478

[46] J. Grandal et al., "Plan-view transmission electron microscopy investigation of GaAs/(In,Ga)As core-shell nanowires", *Applied Physics Letters* **105** (2014) 121602

[47] N. I. Kato, "Reducing focused ion beam damage to transmission electron microscopy samples", *Journal of Electron Microscopy* **53** (2004) 451–458

[48] M. Schaffer, B. Schaffer, and Q. Ramasse, "Sample preparation for atomic-resolution STEM at low voltages by FIB", *Ultramicroscopy* **114** (2012) 62–71

[49] L. A. Giannuzzi and F. A. Stevie, *Introduction to Focused Ion Beams Instrumentation, Theory, Techniques and Practice*, Springer, City of New York, New York, USA (2005)

[50] L. Romano et al., "Nanoscale manipulation of Ge nanowires by ion irradiation", *Journal of Applied Physics* **106** (2009)

[51] J. Mayer, L. A. Giannuzzi, T. Kamino, and J. Michael, "TEM sample preparation and damage", *MRS Bulletin* **32** (2007) 400–407

[52] M. Heiss et al., "Self-assembled quantum dots in a nanowire system for quantum photonics", *Nature Materials* **12** (2013) 439–444

[53] D. Rudolph et al., "Spontaneous alloy composition ordering in GaAs-AlGaAs core-shell nanowires", *Nano Letters* **13** (2013) 1522–1527

[54] A. R. Spurr, "A low-viscosity epoxy resin embedding medium for electron microscopy", *Journal of Ultrastructure Research* **26** (1969) 31–43

[55] L. Lechner, J. Biskupek, and U. Kaiser, "Improved focused ion beam target preparation of (S)TEM specimen - a method for obtaining ultrathin lamellae", *Microscopy and Microanalysis* **18** (2012) 1–6

[56] N. D. Bassim et al., "Minimizing damage during FIB sample preparation of soft materials", *Journal of Microscopy* **245** (2012) 288–301

[57] F. Rivera, R. Davis, and R. Vanfleet, "Alternative FIB TEM sample preparation method for cross-sections of thin metal films deposited on polymer substrates", *Microscopy and Microanalysis* **19** (2013) 1–12

[58] T. Ohnishi et al., "A new focused-ion-beam microsampling technique for TEM observation of site-specific areas", *Conference Proceedings from the International Symposium for Testing and Failure Analysis* ASM International, Novelty, Ohio, USA (1999) 449–453

[59] G. Akasegawa and M. Fargo (Trans.), *Hyperart: Thomasson*, Kaya Press, City of New York, New York, USA (2009)

[60] H. Morkoç, *Nitride Semiconductors and Devices*, Springer, Berlin, Germany (1999)

[61] T. Kouno, M. Sakai, K. Kishino, and K. Hara, "Hexagonal GaN microdisk with wurtzite/zinc-blende GaN crystal phase nano-heterostructures and high quality zinc-blende GaN crystal layer", *Japanese Journal of Applied Physics* **53** (2014)

[62] D. Kriegner et al., "Unit cell structure of crystal polytypes in InAs and InSb nanowires", *Nano Letters* **11** (2011) 1483–1489

[63] D. L. Dheeraj et al., "Growth and characterization of wurtzite GaAs nanowires with defect-free zinc blende GaAsSb inserts", *Nano Letters* **8** (2008) 4459–4463

[64] F. Glas, J. C. Harmand, and G. Patriarche, "Why does wurtzite form in nanowires of III-V zinc blende semiconductors?", *Physical Review Letters* **99** (2007)

[65] P. Caroff, J. Bolinsson, and J. Johansson, "Crystal phases in III-V nanowires: From random toward engineered polytypism", *IEEE Journal of Selected Topics in Quantum Electronics* **17** (2011) 829–846

[66] P. Caroff et al., "Controlled polytypic and twin-plane superlattices in III-V nanowires", *Nature Nanotechnology* **4** (2009) 50–55

[67] X. Yuan et al., "Tunable polarity in a III–V nanowire by droplet wetting and surface energy engineering", *Advanced Materials* **27** (2015) 6096–6103

[68] D. B. Holt, "Grain boundaries in the sphalerite structure", *Journal of Physics and Chemistry of Solids* **25** (1964) 1385–1395

[69] D. B. Holt, "Polarity reversal and symmetry in semiconducting compounds with the sphalerite and wurtzite structures", *Journal of Materials Science* **19** (1984) 439–446

[70] J. Bolinsson et al., "Direct observation of atomic scale surface relaxation in ortho twin structures in GaAs by XSTM.", *Journal of Physics: Condensed Matter* **21** (2009) 055404

[71] M. C. Ridgway and C. S. Schnohr, *X-Ray Absorption Spectroscopy of Semiconductors*, Springer, Berlin, Germany (2015)

[72] S. Fernández-Garrido et al., "Spontaneous nucleation and growth of GaN nanowires: The fundamental role of crystal polarity", *Nano Letters* **12** (2012) 6119–6125

[73] K. Hillerich et al., "Strategies to control morphology in hybrid group III-V/group IV heterostructure nanowires", *Nano Letters* **13** (2013) 903–908

[74] R. L. Barns and W. C. Ellis, "Whisker crystals of gallium arsenide and gallium phosphide grown by the vapor–liquid–solid mechanism", *Journal of Applied Physics* **36** (1965) 2296

[75] K. A. Dick et al., "The morphology of axial and branched nanowire heterostructures", *Nano Letters* **7** (2007) 1817–1822

[76] J. Johansson, B. A. Wacaser, K. A. Dick, and W. Seifert, "Growth related aspects of epitaxial nanowires", *Nanotechnology* **17** (2006)

[77] B. A. Wacaser, K. Deppert, L. S. Karlsson, L. Samuelson, and W. Seifert, "Growth and characterization of defect free GaAs nanowires", *Journal of Crystal Growth* **287** (2006) 504–508

[78] M. Heurlin et al., "Continuous gas-phase synthesis of nanowires with tunable properties", *Nature* **492** (2012) 90–94

[79] N. W. Jepps and T. F. Page, "Polytypic transformations in silicon carbide", *Progress in Crystal Growth and Characterization* **7** (1983) 259–307

[80] N.-H. Cho, S. Mckernan, D. K. Wagner, and C. B. Carter, "Grain boundaries and antiphase bounaries in GaAs", *Journal de Physique Colloques* **49** (1988)

[81] P. Lejček, *Grain Boundary Segregation in Metals*, Springer, Berlin, Germany (2010)

[82] D. Cohen and C. B. Carter, "$\Sigma = 3$, $\{11\bar{2}\}$ lateral twin boundaries in GaP", *Interface Science* **11** (2003) 391–401

[83] M. I. den Hertog et al., "Hidden defects in silicon nanowires", *Nanotechnology* **23** (2012)

[84] E. R. Hemesath, D. K. Schreiber, C. F. Kisielowski, A. K. Petford-Long, and L. J. Lauhon, "Atomic structural analysis of nanowire defects and polytypes enabled through cross-sectional lattice imaging", *Small* **8** (2012) 1717–1724

[85] G. Patriarche et al., "Wurtzite to zinc blende phase transition in GaAs nanowires induced by epitaxial burying", *Nano Letters* **8** (2008) 1638–1643

[86] K. W. Ng, W. S. Ko, F. Lu, and C. J. Chang-Hasnain, "Metastable growth of pure wurtzite InGaAs microstructures", *Nano Letters* **14** (2014) 4757–4762

[87] X. J. Chen, G. Perillat-Merceroz, D. Sam-Giao, C. Durand, and J. Eymery, "Homoepitaxial growth of catalyst-free GaN wires on N-polar substrates", *Applied Physics Letters* **97** (2010)

[88] G. C. Ainsworth, *Introduction to the History of Mycology*, Cambridge University Press, Cambridge, UK (1976)

[89] R. Ramamoorthy, D. Sundararaman, and S. Ramasamy, "Ionic conductivity studies of ultrafine-grained yttria stabilized zirconia polymorphs", *Solid State Ionics* **123** (1999) 271–278

[90] E. Fabbri, D. Pergolesi, and E. Traversa, "Materials challenges toward proton-conducting oxide fuel cells: a critical review", *Chemical Society Reviews* **39** (2010) 4355–4369

[91] F. Lefebvre-Joud, G. Gauthier, and J. Mougin, "Current status of proton-conducting solid oxide fuel cells development", *Journal of Applied Electrochemistry* **39** (2009) 535–543

[92] P. Midgley and R. E. Dunin-Borkowski, "Electron tomography and holography in materials science", *Nature Materials* **8** (2009) 271–280

[93] G. Behan, E. C. Cosgriff, A. I. Kirkland, and P. D. Nellist, "Three-dimensional imaging by optical sectioning in the aberration-corrected scanning transmission electron microscope", *Philosophical Transactions of the Royal Society of London A: Mathematical, Physical and Engineering Sciences* **367** (2009) 3825–3844

[94] A. Magraso and R. Haugsrud, "Effects of the La/W ratio and doping on the structure, defect structure, stability and functional properties of proton-conducting lanthanum tungstate $La_{28-x}W_{4+x}O_{54+\delta}$. A review", *Journal of Materials Chemistry A* **2** (2014) 12630–12641

[95] M. Balaguer, C. Solis, F. Bozza, N. Bonanos, and J. M. Serra, "High performance anodes with tailored catalytic properties for $La_{5.6}WO_{11.4-\delta}$ based proton conducting fuel cells", *Journal of Materials Chemistry A* **1** (2013) 3004–3007

[96] D. Poetzsch, R. Merkle, and J. Maier, "Oxygen reduction at dense thin-film microelectrodes on a proton-conducting electrolyte I. considerations on reaction mechanism and electronic leakage effects", *Journal of The Electrochemical Society* **162** (2015) F939–F950

[97] H. Uchida, S. Tanaka, and H. Iwahara, "Polarization at Pt electrodes of a fuel cell with a high temperature-type proton conductive solid electrolyte", *Journal of Applied Electrochemistry* **15** (1985) 93–97

[98] F. He, T. Wu, R. Peng, and C. Xia, "Cathode reaction models and performance analysis of $Sm_{0.5}Sr_{0.5}CoO_{3-\delta}$–$BaCe_{0.8}Sm_{0.2}O_{3-\delta}$ composite cathode for solid oxide fuel cells with proton conducting electrolyte", *Journal of Power Sources* **194** (2009) 263–268

[99] R. Merkle, D. Poetzsch, and J. Maier, "Oxygen reduction reaction at cathodes on proton conducting oxide electrolytes: contribution from three phase boundary compared to bulk path", *ECS Transactions* **66** (2015) 95–102

[100] J. C. H. Spence and J. Taftø, "ALCHEMI: a new technique for locating atoms in small crystals", *Journal of Microscopy* **130** (1983) 147–154

[101] A. Beche, J. L. Rouviere, J. P. Barnes, and D. Cooper, "Strain measurement at the nanoscale: Comparison between convergent beam electron diffraction, nano-beam electron diffraction, high resolution imaging and dark field electron holography", *Ultramicroscopy* **131** (2013) 10–23

[102] R. Bierwolf et al., "Direct measurement of local lattice distortions in strained layer structures by HREM", *Ultramicroscopy* **49** (1993) 273–285

[103] M. J. Hÿtch, E. Snoeck, and R. Kilaas, "Quantitative measurement of displacement and strain fields from HREM micrographs", *Ultramicroscopy* **74** (1998) 131–146

[104] L. Clément, R. Pantel, L. F. T. Kwakman, and J. L. Rouvière, "Strain measurements by convergent-beam electron diffraction: The importance of stress relaxation in lamella preparations", *Applied Physics Letters* **85** (2004) 651–653

[105] (Music), "The Race for Space", *The Race for Space.* Public Service Broadcasting, J. Willgoose, Esq. (Composer), Test Card Recordings, London, UK (2015)

[106] F. L. Deepak, A. Mayoral, and R. Arenal, *Advanced Transmission Electron Microscopy*, Springer, Switzerland (2015)

[107] T. Sasaki, H. Sawada, F. Hosokawa, Y. Sato, and K. Suenaga, "Aberration-corrected STEM/TEM imaging at 15kV", *Ultramicroscopy* **145** (2014) 50–55

[108] J. P. McCaffrey, M. W. Phaneuf, and L. D. Madsen, "Surface damage formation during ion-beam thinning of samples for transmission electron microscopy", *Ultramicroscopy* **87** (2001) 97–104

[109] S. Rubanov and P. R. Munroe, "FIB-induced damage in silicon", *Journal of Microscopy* **214** (2004) 213–221

[110] M. R. Lee et al., "Characterization of mineral surfaces using FIB and TEM: a case study of naturally weathered alkali feldspars", *American Mineralogist* **92** (2007) 1383–1394

[111] C. A. Volkert and A. M. Minor, "Focused ion beam microscopy and micromachining", *MRS Bulletin* **32** (2007) 389–399

[112] T. Ishitani, K. Umemura, T. Ohnishi, T. Yaguchi, and T. Kamino, "Improvements in performance of focused ion beam cross-sectioning: aspects of ion-sample interaction", *Journal of Electron Microscopy* **53** (2004) 443–449

[113] P. Gasser, U. E. Klotz, F. A. Khalid, and O. Beffort, "Site-specific specimen preparation by focused ion beam milling for transmission electron microscopy of metal matrix composites", *Microscopy and Microanalysis* **10** (2004) 311–316

[114] N. S. Smith, J. A. Notte, and A. V. Steele, "Advances in source technology for focused ion beam instruments", *MRS Bulletin* **39** (2014) 329–335

[115] J. Huang, "Applications of cryo-FIB on Ga-beam sensitive materials", *Carl Zeiss Application Note* (2011)

[116] N. Antoniou, A. Graham, C. Hartfield, and G. Amador, "Failure analysis of electronic material using cryogenic FIB-SEM", *Conference Proceedings from the International Symposium for Testing and Failure Analysis* ASM International, Phoenix, Arizona USA, (2012) 399–405

[117] M. C. Dolph and C. Santeufemio, "Exploring cryogenic focused ion beam milling as a Group III–V device fabrication tool", *Nuclear Instruments and Methods in Physics Research Section B: Beam Interactions with Materials and Atoms* **328** (2014) 33–41

[118] R. Okawa et al., "Stability measurement of ion beam current from argon field ion source", *e-Journal of Surface Science and Nanotechnology* **9** (2011) 371–374

[119] R. D. Kelley, K. Song, B. Van Leer, D. Wall, and L. Kwakman, "Xe^+ FIB milling and measurement of amorphous silicon damage", *Microscopy and Microanalysis* **19** (2013) 862–863

[120] N. Bassim, K. Scott, and L. A. Giannuzzi, "Recent advances in focused ion beam technology and applications", *MRS Bulletin* **39** (2014) 317–325

[121] S. Bauerdick et al., "Multispecies focused ion beam lithography system and its applications", *Journal of Vacuum Science & Technology B* **31** (2013)

[122] S. O. Kucheyev et al., "Effect of ion species on the accumulation of ion-beam damage in GaN", *Physical Review B* **64** (2001)

[123] J. J. Clarke, "A novel approach to TEM preparation with a (7-axis stage) triple-beam FIB-SEM system", *SPIE Scanning Microscopies* **9636** (2015)

[124] W. van Mierlo et al., "Practical aspects of the use of the X^2 holder for HRTEM-quality TEM sample preparation by FIB", *Ultramicroscopy* **147** (2014) 149–155

[125] T. Aoki, "Molecular dynamics simulations of cluster impacts on solid targets: implantation, surface modification, and sputtering", *Journal of Computational Electronics* **13** (2014) 108–121

[126] H. Chen et al., "Smoothing of ZnO films by gas cluster ion beam", *Nuclear Instruments and Methods in Physics Research Section B: Beam Interactions with Materials and Atoms* **241** (2005) 630–635

[127] R. MacCrimmon, J. Hautala, M. Gwinn, and S. Sherman, "Gas cluster ion beam infusion processing of semiconductors", *Nuclear Instruments and Methods in Physics Research Section B: Beam Interactions with Materials and Atoms* **242** (2006) 427–430

[128] E. J. Teo et al., "Sub-30 nm thick plasmonic films and structures with ultralow loss", *Nanoscale* **6** (2014) 3243–3249

[129] H. Kitani, N. Toyoda, J. Matsuo, and I. Yamada, "Incident angle dependence of the sputtering effect of Ar-cluster-ion bombardment", *Nuclear Instruments and Methods in Physics Research Section B: Beam Interactions with Materials and Atoms* **121** (1997) 489–492

[130] Y. K. Kyoung et al., "Damage profiles of Si (001) surface via Ar cluster beam sputtering", *Surface and Interface Analysis* **45** (2013) 150–153

[131] T. Miyayama, N. Sanada, S. R. Bryan, J. S. Hammond, and M. Suzuki, "Removal of Ar^+ beam-induced damaged layers from polyimide surfaces with argon gas cluster ion beams", *Surface and Interface Analysis* **42** (2010) 1453–1457

[132] T. Aoki and J. Matsuo, "Molecular dynamics simulations of sequential cluster ion impacts", *Nuclear Instruments and Methods in Physics Research Section B: Beam Interactions with Materials and Atoms* **228** (2005) 46–50

[133] Z. Insepov, L. P. Allen, C. Santeufemio, K. Jones, and I. Yamada, "Computer modeling and electron microscopy of silicon surfaces irradiated by cluster ion impacts", *Nuclear Instruments and Methods in Physics Research Section B: Beam Interactions with Materials and Atoms* **202** (2003) 261–268

[134] E. Bourelle, A. Suzuki, A. Sato, T. Seki, and J. Matsuo, "Polishing of sidewall surfaces using a gas cluster ion beam", *Japanese Journal of Applied Physics* **43** (2004)

[135] E. Bourelle, A. Suzuki, A. Sato, T. Seki, and J. Matsuo, "Sidewall polishing with a gas cluster ion beam for photonic device applications", *Nuclear Instruments and Methods in Physics Research Section B: Beam Interactions with Materials and Atoms* **241** (2005) 622–625

[136] P. Sigmund, "A mechanism of surface micro-roughening by ion bombardment", *Journal of Materials Science* **8** (1973) 1545–1553

[137] "Climbing Mount Everest is Work for Supermen; A Member of Former Expeditions Tells of the Difficulties Involved in Reaching the Top – Hope of Winning in 1924 by Establishment of Base Camps on a Higher Level.", *The New York Times* (1923, March 18) page 11 in Section 7

[138] G. Hägg, *Allmän och oorganisk kemi*, Almqvist & Wiksell, Uppsala, Sweden, 4th edition (1966)

[139] J. H. Orloff, "Study of a field-ionization source for microprobe applications", *Journal of Vacuum Science & Technology* **12** (1975) 1209

[140] W. H. Escovitz, T. R. Fox, and R. Levi-Setti, "Scanning transmission ion microscope with a field ion source", *Proceedings of the National Academy of Sciences of the United States of America* **72** (1975) 1826–1828

[141] R. L. Seliger, J. W. Ward, V. Wang, and R. L. Kubena, "A high-intensity scanning ion probe with submicrometer spot size", *Applied Physics Letters* **34** (1979) 310–312

[142] P. Grivet and A. Septier, "Ion microscopy: History and actual trends", *Annals of the New York Academy of Sciences* **306** (1978) 158–182

[143] D. C. Joy and J. R. Michael, "Modeling ion-solid interactions for imaging applications", *MRS Bulletin* **39** (2014) 342–346

[144] J. R. A. Cleaver, E. C. G. Kirk, R. J. Young, and H. Ahmed, "Scanning ion beam techniques for the examination of microelectronic devices", *Journal of Vacuum Science & Technology B* **6** (1988) 1026

[145] E. C. G. Kirk, D. A. Williams, and H. Ahmed, "Cross-sectional transmission electron microscopy of precisely selected regions from semiconductor devices", *Institute of Physics Conference Series 100* Institute of Physics Publishing, Philadelphia, Pennsylvania, USA, (1989) 501–506

[146] M. H. F. Overwijk, F. C. van den Heuvel, and C. W. T. Bulle-Lieuwma, "Novel scheme for the preparation of transmission electron microscopy specimens with a focused ion beam", *Journal of Vacuum Science & Technology B* **11** (1993)

[147] L. A. Giannuzzi, J. L. Drown, S. R. Brown, R. B. Irwin, and F. A. Stevie, "Focused ion beam milling and micromanipulation lift-out for site specific cross-section TEM specimen preparation", *MRS Proceedings* **480** (1997) 19

[148] M. Cantoni and L. Holzer, "Advances in 3D focused ion beam tomography", *MRS Bulletin* **39** (2014) 354–360

[149] P. G. Kotula, G. S. Rohrer, and M. P. Marsh, "Focused ion beam and scanning electron microscopy for 3D materials characterization", *MRS Bulletin* **39** (2014) 361–365

Acknowledgements

This thesis was made possible thanks to the aid of many people. First, I would like to thank my supervisor Reine. You have guided me through everything from hosting an art exhibition to writing this. I would also like to thank Staffan, my co-supervisor. I love how you sent me on a neverending hunt for dreikanters and I was excited to share the hyperart of Thomassons with you.

Without the members of the microscopy group Axel, Crispin, Gunnel, Kimberly and Martin, this thesis would not have been possible. You were my teachers and sounding boards when I processed difficult microscopy concepts. Alexander, Bi, Camilla, Daniel, David, Jason, Jonas, Magnus, Mariano, Maryam, Mikael, Nikos, Per Martin, Rafal, Sandrine, Sebastian, Theo and Volodymyr are thanked for sharing your samples with me. Without them this would be an empty thesis. Many thanks to the staff at Lund Nano Lab for their hard work. I am truly grateful. Thanks to the colleagues at the Centre for Analysis and Synthesis. You made fika the highlight of each day, not to mention the occasional after-work. Collaborators and friends at Solid State Physics and Synchrotron Radiation are acknowledged. I highly appreciate your invaluable contribution.

Annika, Emelie and Maria, we have shared lunches full of laughs and peptalk. Thank you for all your support and encouragements. Erik and Martin...what can I say? We have been through a lot together, from tower beer, pizza roulette, and der schwarze Hahn to passing Zemst, hunting WiFi and eating snoep. Thanks to Hans and Sven with colleagues at SUS and USÖ, for all your work and effort.

Sigrid, you have been everything to me, from a teenage love to my life companion. Hilda and Vera, my darling girls, you have brought more joy into my life than I thought possible.

This work was supported by the Nanometer Structure Consortium at Lund University, along with Energimyndigheten, project no: 38328-1 and no: 32939-1, the N-INNER-program.